
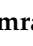


Article

Metallogeny and Genesis of Fault-Filling Barite-Sulfide Veins (Ougnat, Morocco): Petrography, Fluid Inclusion, and Sr-S Isotopic Constraints

Samir Samaoui ^{1,*}, Ayoub Aabi ², Abdellah Boushaba ³, Belkasmi Mohammed ¹, Abdellah Nait Bba ⁴, Abderrahim Essaifi ⁵, Lahssen Baïdder ⁶ and Othmane Lamrani ³

- ¹ Laboratory of Geosciences, Environment and Associated Resources, Faculty of Sciences Dhar El Mahraz, Sidi Mohamed Ben Abdellah University, Fez 30000, Morocco; mohammed.belkasmi@usmba.ac.ma
- ² Department of Earth Sciences, Ecole Normale Superior, Mohammed-V University, Rabat 10000, Morocco; a.aabi@um5r.ac.ma
- ³ Laboratory of Natural Substances, Pharmacology, Environment, Modeling, Health & Quality of Life, Faculty of Sciences Dhar El Mahraz, Sidi Mohamed Ben Abdellah University, Fez 30000, Morocco; abdellah.boushaba@usmba.ac.ma (A.B.); othmane.lamrani@usmba.ac.ma (O.L.)
- ⁴ Mineral Deposits, Hydrogeology & Environment Laboratory, Department of Geology, Faculty of Sciences, Mohammed I University, Oujda 60000, Morocco; a.naitbba@ump.ac.ma
- ⁵ Department of Geology, Faculty of Sciences Semlalia, B.P. 2390, Marrakech 40000, Morocco; essaifi@uca.ac.ma
- ⁶ Department of Geology, Faculty of Sciences Ain Chock, Hassan II University, Casablanca 20100, Morocco; lahssen.baïdder@etu.univh2c.ma
- * Correspondence: samir.samaoui@usmba.ac.ma; Tel.: +212-662-163677

Abstract: The Ougnat Massif of the eastern Anti-Atlas (Morocco) hosts barite and sulfide vein-type deposits of vital economic importance. With over 150 mineralized structures reported in the Ougnat Massif, the ore-bearing ones are predominantly composed of barite, quartz, calcite, and minor portions of sulfides. The mineralized veins are driven by NW-SE and NE-SW to E-W oblique-slip opening faults that cross both the Precambrian basement and its Paleozoic cover. The mineralized structures occur as lenses and sigmoidal veins that follow stepped tension fracture sets oblique to the fault planes. These geometries and kinematic indicators of these structures point to a predominantly normal-sinistral opening in a brittle-ductile tectonic setting. The S isotopic compositions of barite from the Ougnat Massif (+10.8 to +19.5‰) fall mostly within the range of $\delta^{34}\text{S}$ values of Late Triassic to Jurassic seawater, thus suggesting that some of the SO_4^{2-} in barite comes from seawater sulfate. This range of $\delta^{34}\text{S}$ values also corresponds approximately to the hydrothermal barite context. The $^{87}\text{Sr}/^{86}\text{Sr}$ ratios of barite, which range from 0.710772 to 0.710816, lie between the radiogenic strontium isotopic compositions of deposition by hydrothermal solutions, and also coincide with the non-radiogenic isotopic signature of Triassic to Jurassic seawater. Based on a fluid inclusions study, the ore-forming fluids were a mixture of two or more fluids. A deep hot fluid with an average temperature of 368 °C leached the granodiorites and volcanic-sedimentary complex of the Ouarzazate Group. This fluid provided the hydrothermal system with most of the Ba, radiogenic Sr, and some of the dissolved S. A second, shallow fluid with an average temperature of 242 °C was derived from Late Triassic to Jurassic seawater. The barite mineralization of the Ougnat Massif constitutes a typical example of vein-type mineralization that occurred along the northern margin of the West African Craton and regionally tied to the central Atlantic opening.

Keywords: barite veins; fluid inclusions; sulfur isotopes; strontium isotopes; tectonic; Ougnat Massif; Anti-Atlas

1. Introduction

Barite holds significant value in industries such as aerospace, chemicals, and petroleum, as well as for the production of white goods [1–11]. Thanks to its versatility in these fields of



Citation: Samaoui, S.; Aabi, A.; Boushaba, A.; Mohammed, B.; Nait Bba, A.; Essaifi, A.; Baïdder, L.; Lamrani, O. Metallogeny and Genesis of Fault-Filling Barite-Sulfide Veins (Ougnat, Morocco): Petrography, Fluid Inclusion, and Sr-S Isotopic Constraints. *Geosciences* **2024**, *14*, 83. <https://doi.org/10.3390/geosciences14030083>

Academic Editor:
Jesus Martinez-Frias

Received: 25 January 2024
Revised: 9 March 2024
Accepted: 13 March 2024
Published: 18 March 2024



Copyright: © 2024 by the authors. Licensee MDPI, Basel, Switzerland. This article is an open access article distributed under the terms and conditions of the Creative Commons Attribution (CC BY) license (<https://creativecommons.org/licenses/by/4.0/>).

application, it contributes significantly to the national economy. With an annual production of 1100 metric tons, Morocco is the seventh-largest producer of barite in the world [4] (Table 1).

Table 1. Production resources of barite in major countries from 2016 to 2022 (metric tons).

Particular Year	2016	2017	2018	2019	2020	2021	2022
China	2800	3100	3200	2900	2500	2100	1900
Kazakhstan	482	500	620	620	600	450	500
Turkey	170	200	290	250	130	258	300
India	1050	1100	2000	2200	2000	1600	2600
Iran	480	500	550	490	200	224	220
United States	240	NA	480	390	NA	NA	NA
Morocco	107	140	1000	1100	800	1100	1300
Mexico	197	140	400	400	280	321	320
Pakistan	107	140	110	110	110	-	-
Thailand	223	148	150	NA	NA	-	-
Russia	434	430	220	160	160	-	-
Other	470	470	460	900	340	528	580
Global	7320	7700	9480	9520	7500	6730	7900

Data source: U.S. Geological Survey, Mineral Commodity Summaries, January 2023; NA said no statistics.

However, despite this obvious economic importance, the study of barite deposits genesis in Morocco remains very limited [12–21]. Barite deposits are widely distributed over the whole Moroccan territory, hosted in various geological formations of varying nature and age [14,22]. Three main types of barite deposits have been studied in Morocco, based on their shape of mineralization (stratiform, karstic, and vein deposits) [14,16,22,23] (Figure 1). Stratiform mineralization is rare and limited, and can only be seen embedded within the Lower Paleozoic formations of the High Atlas [16]. Karstic mineralization is exploited in the western Paleozoic Meseta, notably at the Jebel Irhoud mine [20,22] and Bou Ouzel mine [15]. Barite vein deposits are mined extensively throughout the structural domains of Morocco, spanning from the southern Anti-Atlas belt, including the Ougnat Massif, to the northern Cenozoic Rif mountains (Figure 1).

Field-based structural constraints suggest that the vein-type barite deposits in the High Atlas, Eastern Anti-Atlas, and western Meseta of Morocco, formed in response to an extensional tectonic context related to the Central Atlantic opening [15–19,21,24–26]. These deposits could be genetically correlated to certain barite deposits in central and western Europe [23,27–32]. From a metallogenic point of view, the only research carried out in the Ougnat Massif (Eastern Anti-Atlas) has successfully discussed the genesis process of the Bou Madine Au-Ag-Pb-Zn ± Cu deposit as an epithermal-type deposit [33,34].

Studies on barite from the Ougnat Massif (Figure 2) have been relatively scarce, with only a few notable studies including. [35], used electrical tomography to define the alignment of barite veins with galena. However, Ref. [36] have discussed the environmental impacts of barite mining in the Ougnat Massif. Recently, Ref. [18] discussed the genetic relationships between faults and barite veins, describing that the barite of the Ougnat Massif is vein-type, and that mineralization-bearing structures are hosted within NE-SW to E-W and NW-SE strike-slip-normal fault system. In contrast to well-studied European deposits such as those in the Catalonian Coastal Ranges (Spain), Western Erzgebirge (Germany) and Sardinia (Italy) [36–41], where mineralogy, fluid chemistry, and emplacement ages are thoroughly documented, the barite deposits in Morocco are relatively understudied from a metallogenic perspective. The present, study therefore, aims to investigate, for the first time, fluid inclusions in barite from the Ougnat Massif by combining Sr and S isotopes to (1) characterize vein-type barite mineralization, (2) establish the fluid pathway and source responsible for ore formation, (3) and understand the genetic process of the ore. This research furnishes valuable insights into fault-controlled barite mineralization,

thereby enhancing exploration possibilities for comparable deposits across diverse regions, encompassing the Paleozoic cover of the entire Anti-Atlas.

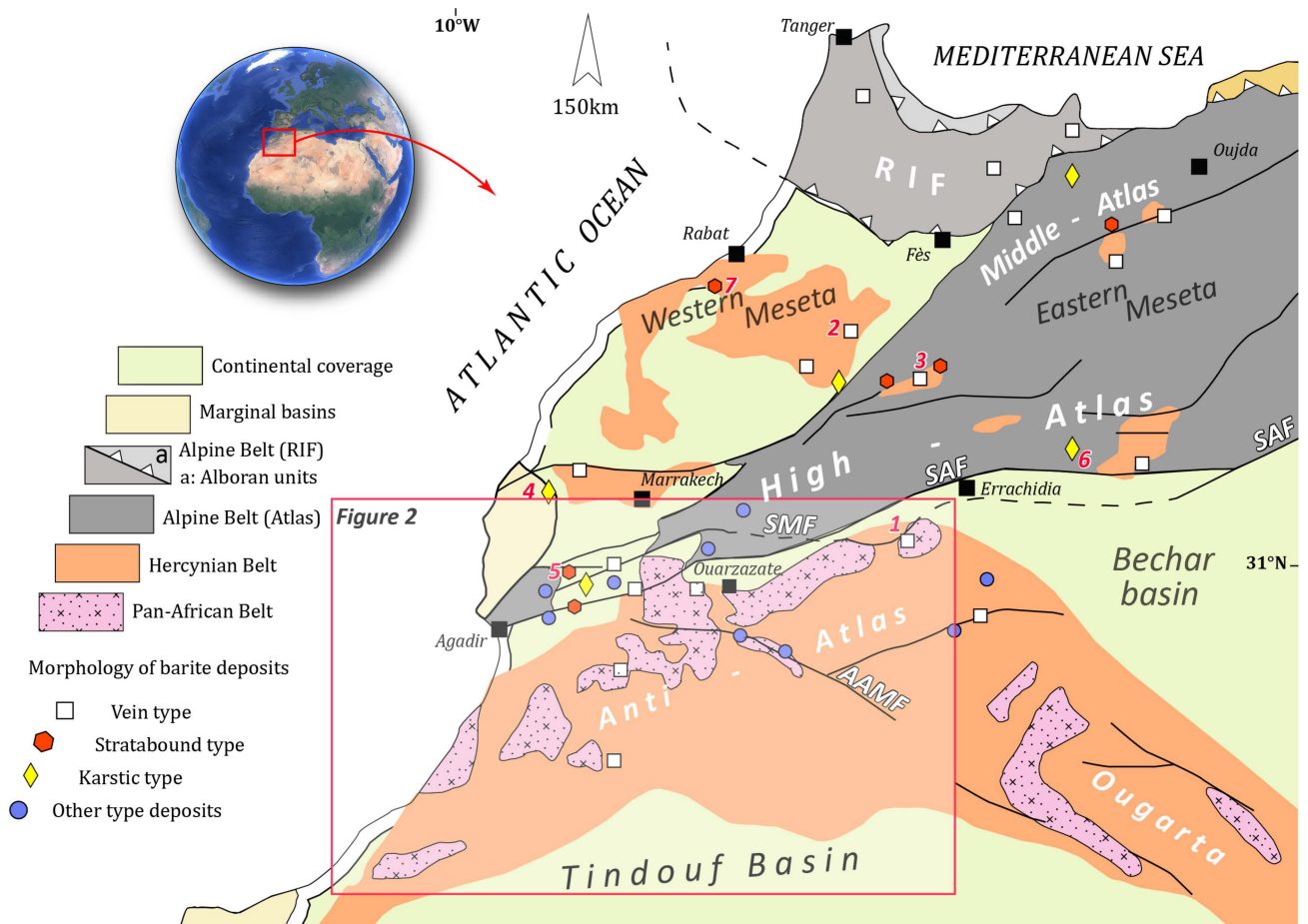


Figure 1. Spatial distribution of the main barite deposits in the Atlas-Meseta and the Anti-Atlas domains [22,37]. AAMF: Anti-Atlas Major Fault, SMF: South Mesetian Fault, SAF: South Atlasic Fault, 1: Ougnat deposit, 2: Bou Ouzzal deposit, 3: Aouli deposit, 4: Jbel Irhoud deposit, 5: Sekksaoua deposit, 6: Zelmou deposit, and 7: Bouznika deposit.

2. Geologic Setting

The Anti-Atlas belt of Morocco forms a broad crustal bulge extending in an ENE-WSW direction at the northern fringe of the West African Craton (WAC) (Figure 2). It is bordered to the south by the Carboniferous basin of Tindouf and to the north by the southern margin of the High Atlas. The Saghro and Ougnat Massifs (inliers), located in the eastern part of the Anti-Atlas, constitute important anticlinal structures composed of a deformed Proterozoic basement partially overlain by Paleozoic formations, thus hosting several important mineral-rich deposits [16,34,38–42].

Folding and faulting of the Paleozoic series are attributed to the Variscan and partially Alpine orogenies [37,39,43–46]. The current elevation of the eastern Anti-Atlas, reaching approximately 2700 m in the Jbel Amalou n'Mansour of the Saghro Massif, is due to the latest Atlasic-Alpine shortening [47]. The Saghro and Ougnat Massifs, part of the Pan-African orogenic system, extend northward from the Anti-Atlas Major Fault (AAMF) where the Siroua and Bou Azzer ophiolites as well as the oceanic arc units occur [48–52]. The oldest rocks in the eastern Anti-Atlas belt consist of turbidites and clastic sediments of the Lower Ediacaran, belonging to the Saghro Group. They are unconformably overlain by the late Ediacaran volcanic and volcano-sedimentary rocks of the Ouarzazate Group [53–56].

The Saghro Group in the Ougnat Massif outcrops to the northeast in the Mellab and Ighrane domes [56] (Figure 3). It consists of a series starting with rhythmic alternations of fine-grained sandstones with centimeter to decimeter thickness, fine-grained sandstones, arkoses, greywackes, and interbedded quartzwackes [56]. This group is generally deformed, schistose, and weakly metamorphosed in the greenschist to chlorite and sericite facies during the Pan-African/Cadomian orogeny [57–59]. The granitoids of the Ougnat Massif, which intrude the Saghro group, present two distinct petrographic facies: (i) quartz diorite and (ii) granites [60,61]. The emplacement of these granitoids is assumed to be synchronous [33,60,62–65], which led to contact metamorphism marked by characteristic minerals such as biotite, cordierite, andalusite, and garnet in the metasedimentary series [36]. The Upper Ediacaran Ouarzazate Group features a thick sequence of volcanic caiaand volcano-sedimentary rocks associated with huge plutonic masses [46,49,66–69]. According to Abia et al. [33], Pail. [70], and Radi et al. [71], this sequencepail includes the following units from bottom to top: (i) conglomerates with angular and heterometric elements, formed from erosion of metasedimentary series and granitoids; (ii) the Tamerzaga Formation, composed of an ignimbritic stack and intercalated andesitic lava flows; (iii) the Ouin Oufroukh Formation, which includes sedimentary and volcano-sedimentary rocks such as limestone, chert, mudstone, sandstone, conglomerate, as well as rhyolite and andesite levels; (iv) the Aoujane Aïssa Formation, where ignimbritic rocks dominate with intercalations of dacitic and basaltic lava flows.

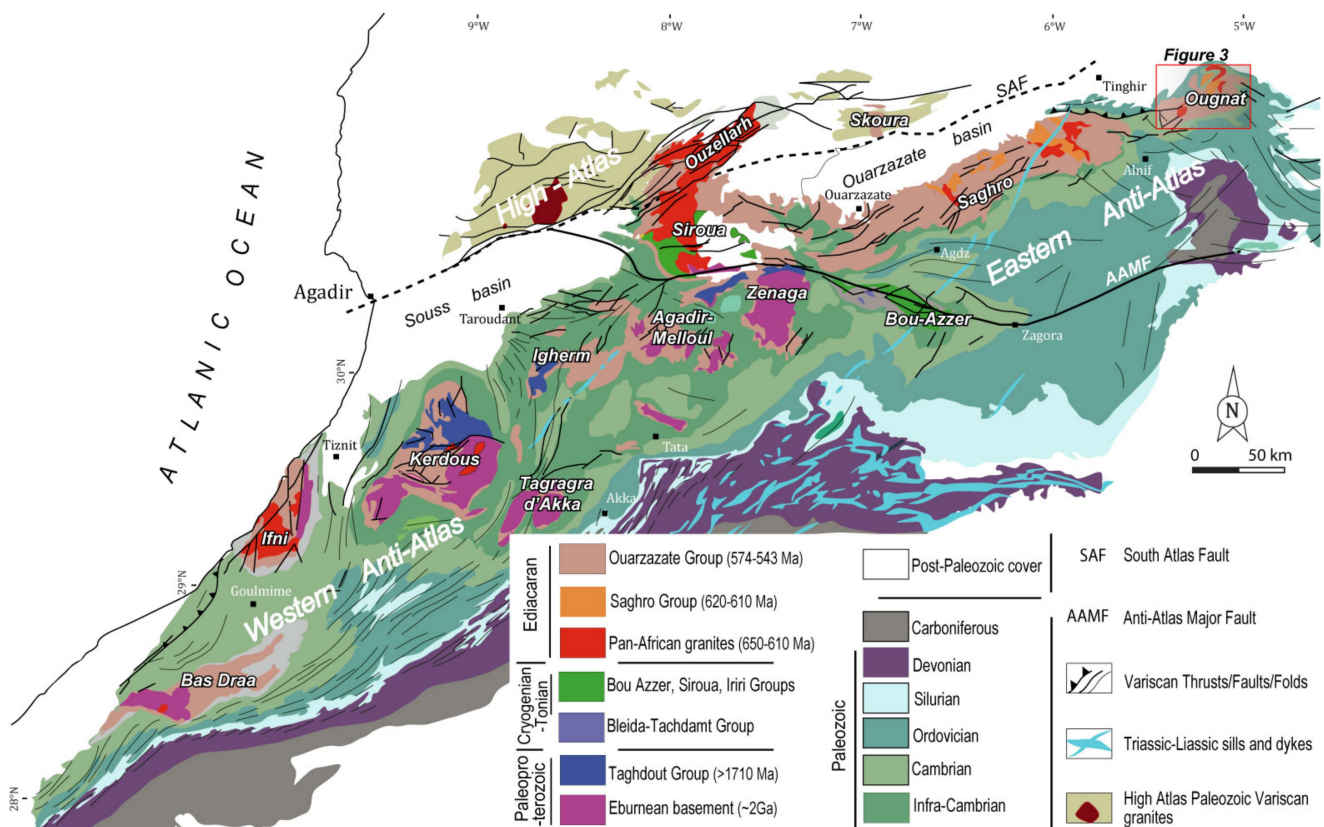


Figure 2. Geological map of the Anti-Atlas belt [37,44,72].

The Paleozoic cover unconformably overlays the Precambrian basement, which begins with the deposition of Lower Cambrian sandstones, known as “Grès Terminaux” [73,74]. In the middle Cambrian, fine-grained sediments were deposited together with alkaline basalt flows [43,44,59]. The Upper Cambrian represents a possible hiatus [75,76] which was followed by a resumption of clastic sedimentation that persisted until the Upper Ordovician. Silurian black shales with graptolites accumulated throughout the region in response to a

post-glacial eustatic transgression after the Saharan glaciation in the Upper Ordovician [77]. During Late Silurian–Devonian, sedimentation became more carbonate-rich [59,77].

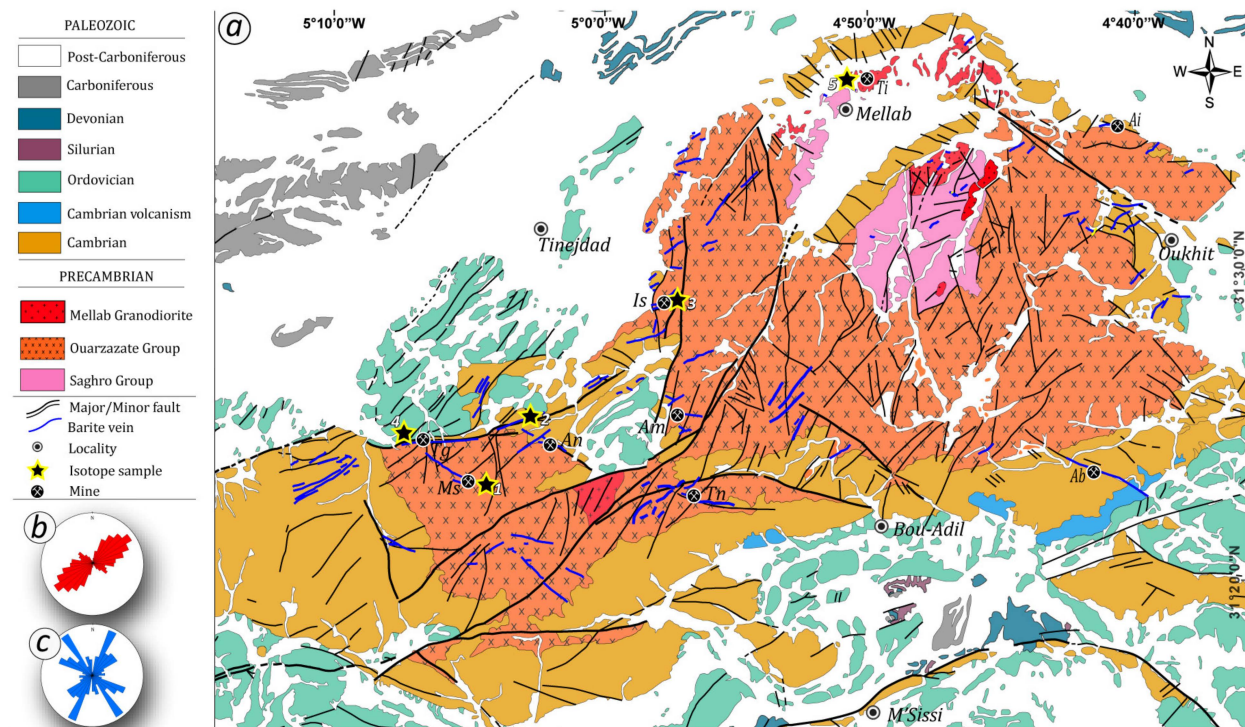


Figure 3. (a) Geological map of the Ougnat Massif [78–80]. Rose diagrams of faults bearing barite vein (b) and mapped faults (c). Tg: Taggat; Ms: Mouassae; An: Ansmine; Am: Amda; Tn: Tinchramine; Is: Isk n'Oudaden; Ti: Tismaght; Ai: Aghri n'Imacher; Ab: Aberchane. 1, 2, 3, 4, and 5: Isotope sample number.

3. Deposit-Scale Barite Vein Description

The Ougnat Massif constitutes one of the important barite metallogenic provinces in North Africa, with over one hundred and fifty barite veins mapped over Precambrian and Paleozoic basement. The most significant barite-bearing structures in the Ougnat Massif are localized along NW-SE and NE-SW to E-W oriented faults (Figure 3). These faults are particularly visible along numerous Precambrian–Paleozoic contact zones, thus considered weak zones that facilitate the mineralized fluid flow. The mineralized structures have length dimensions of a few hundred meters. However, it is common for several structures to occur consecutively along the same fracture. This is particularly the case when these extensional cracks meet almost continuously, when the rock is competent enough to allow larger openings. For instance, at the Tiberguente deposit, which is hosted by Middle Cambrian sandstones, mineralized faults extend over a distance of more than 8 km, whereas at the Taggat mine they extend over more than 12 km along the basement-cover contact zone (Figure 3). The thickness of the structures is variable from place to place, and also depends on the nature of the host rock; generally, of the order of 1 to 2 m (Figure 4a), they can reach a few meters in the largest veins and exceptionally up to 6 m at the Tichramine mine. Vein depths also vary according to their extent, ranging from a few dozen meters to over a hundred meters for the largest veins, e.g., the Mouassaie vein currently being mined at −110 m depth. In some places, the mineralized veins may occur as pairs of conjugate veins and stepped tension fractures. Ore-rich barite deposits, characterized by increasing thickness and high ore concentration, are typically confined to tectonic nodes, where several mineralized structures intersect. Barite mineralization appears as sigmoidal lenses within lithological contact zones, interpreted as stratigraphic boundary structures. It can also take the form of stepped tension fractures set obliquely to the planes of the mineralized faults. Structural data conducted by [18] have shown that the

geometry of these structures shows tectonic kinematics of sinistral–normal opening in a brittle–ductile regime along the host faults, revealed at both microscopic and macroscopic scales. The veins are mainly composed of barite, although other minerals such as calcite, quartz, galena, and, in some places, malachite and azurite may be present (Figure 4e–h). From a textural point of view, barite occurs as massive aggregates or white to pink crested crystals, which are filled within the body. Carbonates are practically absent, but quartz can be abundant.

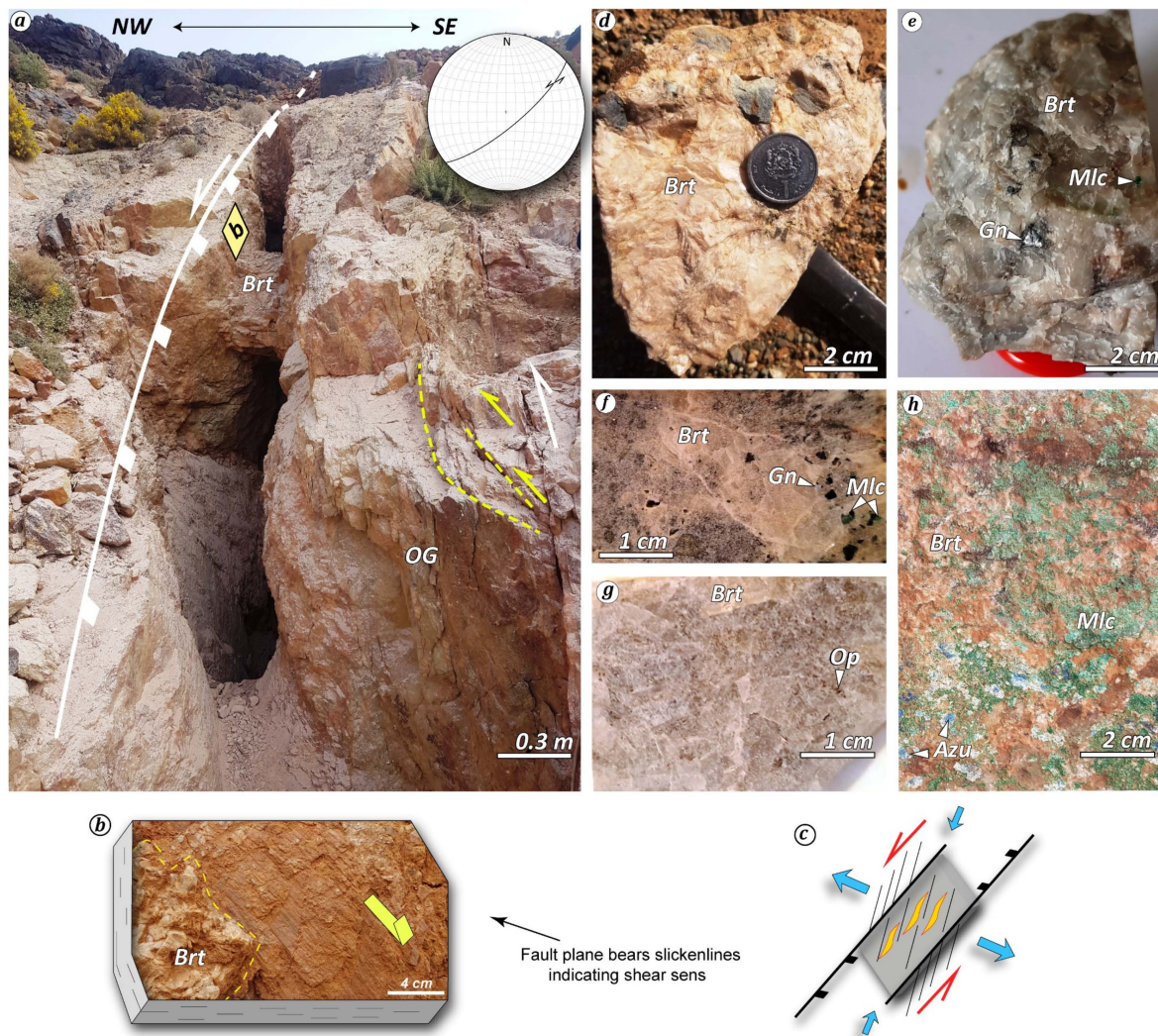


Figure 4. (a) Panoramic view of a sub-vertical mined barite vein, showing tectonics criteria of sinistral–normal kinematics within the Ediacaran Ouarzazate group. (b) Plan of fault-bearing unstriated barite record slickenlines pointing to a dip-slip tectonic opening. (c) Schematic drawing showing transtensional tectonic control of hydrothermal barite veins. (d) Massive white barite displaying large tabular crystals and exhibiting oxidation stains. (e–g) Grey barite containing lead sulfides, malachite, and oxidation stains. (h) Fault mirror featuring pink barite with malachite and azurite. OG: Ouarzazate Group, Brt: barite, Gn: galena, Mlc: malachite, Azu: azurite, and Op: oxidation stains.

4. Methodology

Field-based studies were conducted to establish the relationships among the mineralized vein field, the host rock, and their structures during the precipitation of barite mineralization. Barite samples were collected for petrographic studies (thirty samples), coupled Scanning Electron Microscopy (SEM) and Energy-Dispersive X-ray analysis (EDX) (ten samples), strontium and sulfur isotopic analysis (five samples for both $^{87}\text{Sr}/^{86}\text{Sr}$ and $\delta^{34}\text{S}$, respectively), and microthermometric studies of fluid inclusions (50 measurements).

SEM combined with EDX enabled us to (i) examine the texture and microscopic structure of the samples after carbon metallization and (ii) perform surface microanalysis and qualitative multi-elemental analysis [81]. These analyses were carried out on a Quanta 200 FI SEM equipped with the EDAX probe model JEOL JSM-IT500HR/LA, with different vacuum modes (high vacuum, low vacuum, and ESEM). It had a resolution of 3.5 nm, an acceleration voltage of 0.5 to 30 KV, and 4 fully motorized axes. The EDX analyzer come with Genesis 2000 I software for integration with the Quanta.

Strontium isotope analyses were carried out at Activation Laboratories in Canada, on barite powder samples. These powders were reacted with Milli-Q water for 24 h at 100 °C and the solution dried. Chemical separation procedures for Sr follow the methodology of [82] and [83]. Isotopic analysis for Sr used MC-ICPMS methods. All analyses are presented relative to a value of 0.710245 for the SRM 987 Sr isotopic standard [82]. Sulfur isotopic analyses were performed using Isotope Ratio Mass Spectrometry (IRMS)—MAT 253, Thermo Scientific, coupled with Elemental Analyzer (EA), and Fisons Instruments at the Activation Laboratories in Canada. For the barite samples, the isotopic ratio was calibrated against the barite standards NBS 127, IAEA-SO-6, and IAEA-SO-5 [82]. Therefore, the analytical error of $\delta^{34}\text{S}$ values was less than $\pm 0.5\%$.

Microthermometric measurements of fluid inclusions were conducted using the Chaix Meca stage at Cadi Ayyad University in Morocco [84]. To calibrate the fluid inclusions, we used three types of synthetic fluid inclusions: (i) $\text{H}_2\text{O}-\text{CO}_2$ fluid inclusions with a CO_2 melting temperature (T_{fCO_2}) of -56.6 °C, (ii) pure H_2O fluid inclusions with an ice melting temperature (T_{fg}) of 0.0 °C and a critical homogenization temperature (T_{h}) of 374.1 °C, and (iii) $\text{H}_2\text{O}-\text{NaCl}$ fluid inclusions with a eutectic temperature (T_{e}) of -21.2 °C. We chose these types of inclusions because they allow for accurate calibration of the instruments. The measurement accuracy was ± 0.1 and ± 0.5 °C for temperatures below 0 °C and around 400 °C, respectively. According to Ulrich et al. [85], fluid inclusions in barite can stretch beyond 10 °C of their homogenization temperature. In our process, we measured only fluid inclusions that had not stretched during their homogenization temperature.

5. Results

5.1. Barite Characterization: Textures, Petrography, Paragenesis, and SEM

Textural analysis of the various barite mineralizations discovered in the Ougnat Massif revealed several textures (Figure 5). (i) Massive texture is the most dominant across the veins of the Ougnat Massif (Figure 5a,d). It is frequently represented by large plate-like or centimeter-scale tabular crystals or automorphic orthorhombic crystals (Figure 5a) of varying sizes due to uniform growth rates. It typically appears as white, pink, or gray masses (Figure 5d). (ii) Breccia texture: two different types of breccias were identified, tectonic breccia and hydrothermal breccia. The former is easily recognizable in the field due to grain reduction and fragment orientation. The latter is characterized by more or less rounded fragments of barite and host rocks (Figure 5c), cemented by a hydrothermal matrix. (iii) Banded texture is sparsely developed throughout the Massif, displaying palmate layers of white and pink barite associated with iron and manganese oxides to form alternating bands (Figure 5e). Generally, banded textures indicate a context of intermittent and slow opening of mineralized veins [86,87], in an extensional tectonic environment. (iv) Crested texture extends in several locations along the mineralized structures, consisting of gathered flattened tabular crystal facets (Figure 5f).

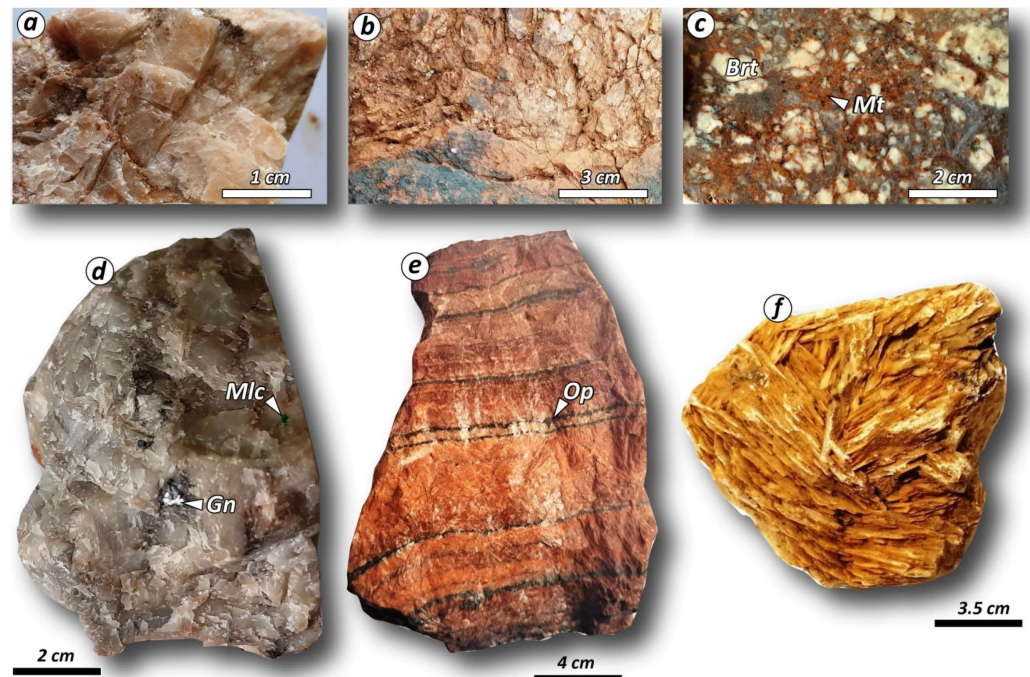


Figure 5. Hand specimen photographs of barite mineralization: (a) massive with orthorhombic automorphs; (b) tectonically brecciated; (c) brecciated; (d) massive; (e) banded; (f) crested. Brt: barite, Gn: galena, Mlc: malachite, Op: oxidation stains, and Mt: matrix.

The barite veins of the Ougnat Massif contained 80–90 vol% barite, ~10–20 vol% quartz-calcite, and ~1 vol% sulfide minerals in the form of galena, chalcopyrite, and their oxidation minerals (malachite, azurite, iron oxide, and manganese oxide). Due to the remobilization of silicates and sulfides along fractures by hydrothermal fluids, significant network textures have been observed in barite. Microscopically, barite appears as elongated, curved, intertwined, and interlocking long prismatic rods with rolling extinction (Figure 6a–e). The cleavages are perfect on (001), nearly perfect on (210), and good on (010) with weak pleochroism. Galena is the most common sulfide in this paragenesis. It forms isolated replacement masses, reaching sizes of a few centimeters, and is disseminated within barite and sometimes in fine veinlets. It is characterized by a good polish and triangular fractures (Figure 6c,d). Chalcopyrite was only found in certain samples (Figure 6h), especially in the Amda mine. It was sparsely present on the surface of veins and forms irregular and xenomorphic patches. Chalcopyrite inclusions in barite are often altered into copper oxides. Late-stage silica, iron oxides, manganese oxides, and hydroxides originate from the cleavages of barite (Figure 6d,f,i).

Macroscopic and microscopic analysis revealed the existence of two distinct generations of barite, each with specific characteristics. (i) Barite I, which is the most predominant type of barite. This first generation can be observed throughout the Ougnat Massif. It takes the form of laths and aggregates of variable size, often with a pink color. The texture of this barite can be massive or stockwork-like. (ii) Barite II forms later than the first and quartz, as it is unaffected by silicification. It takes the form of flattened tablets, with gradual color zonation from dark sandstone to white. Three-stage paragenesis has been recognized based on mineralogical, textural, and cross-cutting relationships. Stage I is the most economically important, accounting for over 80% of the total barite resources, e.g., the Tinchramine mine, with over 760,000 tons of barite stock [18]. The mineral paragenesis consists of barite, quartz, calcite, and very rarely fluorite. Stage II consists of variably colored, centimeter-sized barite occurring in crests and is associated with galena and other sulfides. It also includes fluorite and drusy quartz crystals. Stage III is the result of primary sulfide oxidation and comprises minor amounts of cerussite, malachite, azurite, and iron and manganese oxides (Figure 7).

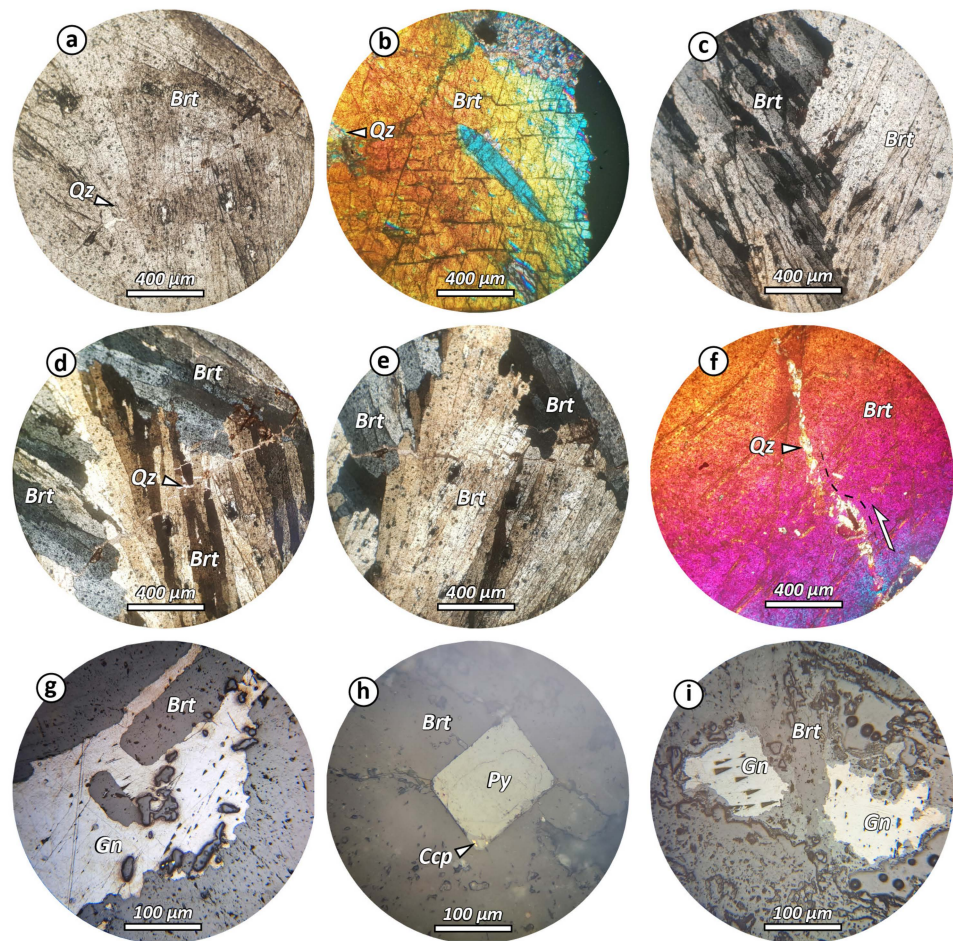


Figure 6. Photomicrographs illustrating textural relationships of barite and associated minerals in the Ougnat Massif. (a–e) Optical microscope photomicrographs with transmitted light of barite showing euhedral grains associated with quartz. (f) Photomicrograph showing a network of quartz-filled veins within the barite. (g–i) Optical microscope photomicrographs with reflected light of barite associated with sulfides. Brt: barite, Qz: quartz, Gn: galena, Ccp: chalcopyrite and Py: pyrite.

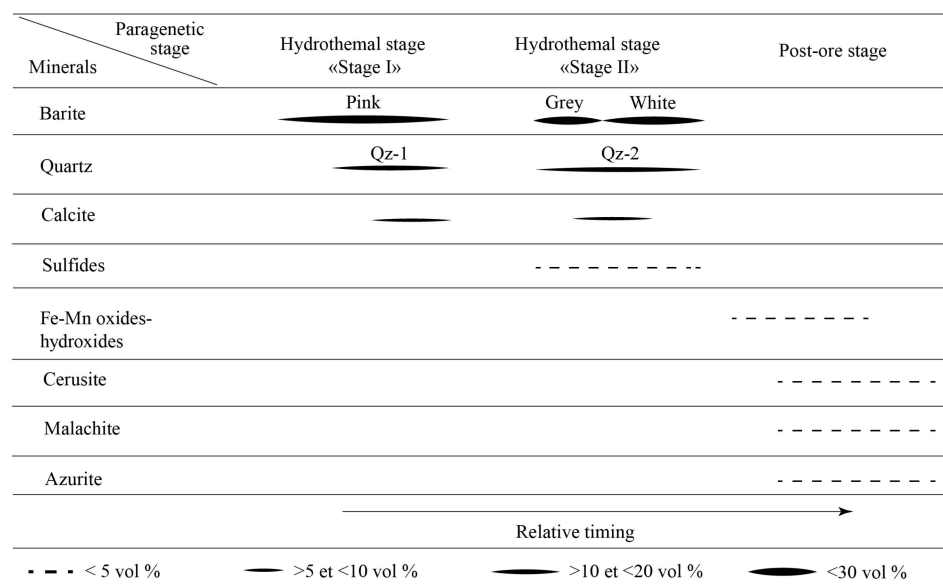


Figure 7. Summary of the paragenetic sequence illustrating the various hydrothermal stages depicted in the Ougnat Massif. The width of the bars is roughly proportional to the intensity or volume event.

To better define the internal structure of barite, the scanning electron microscopy (SEM) technique was applied to visualize the crystal arrangements. When observed using SEM, barite often appears as a massive texture (Figure 8a,b), meaning it appears as a compact mass of crystals with apparent crystal structure; this texture is the most dominant among the studied barite. Barite can also, rarely, be observed as individual crystals, exhibiting characteristic shapes and well-defined crystal structures, elongated or tabular crystals, often in aggregates (Figure 8c,d). In the case of the studied samples, the presence of SiO_2 (Figure 8e) indicates silicification due to hydrothermal activity.

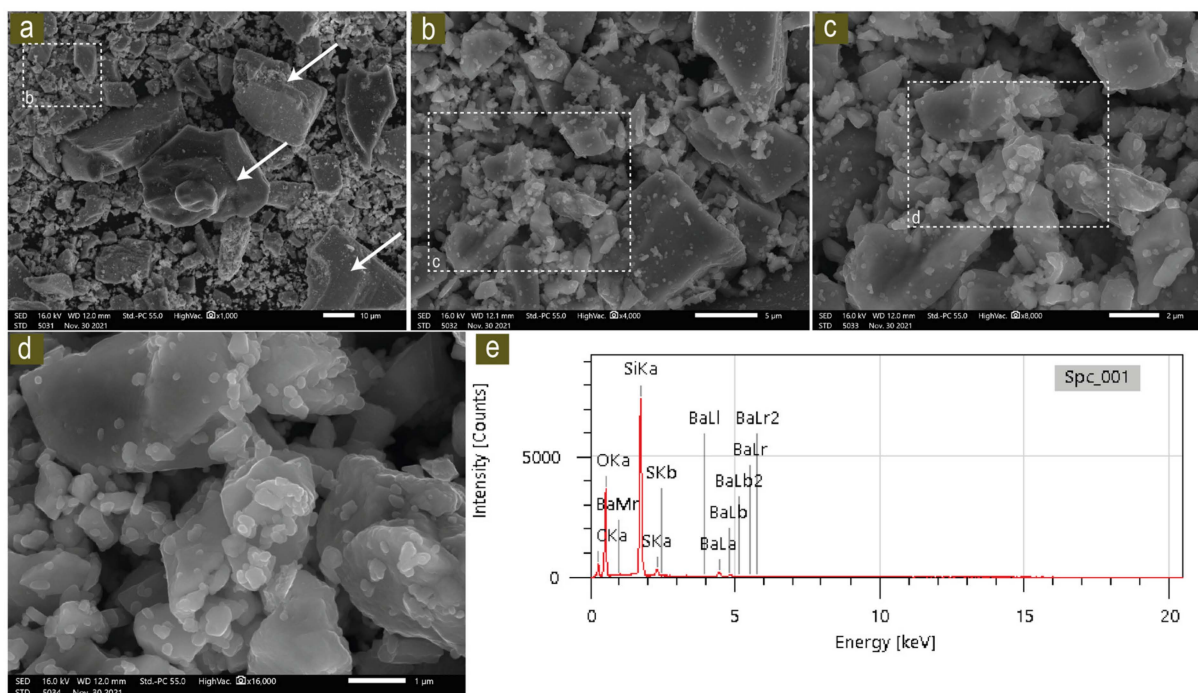


Figure 8. BSE images and EDX spectroscopy of barite from the Amda deposit. (a) fragments of massive textured-barite (arrows); (b–d) micron-scale barite flakes agglomerates; (e) EDX spectra of studied barite showing the presence of an SiO_2 phase.

5.2. Sulfur Isotopes

The sulfur isotopic compositions were obtained for five representative samples of barite. These barite samples were collected from the main mineralized structures hosted both in the Precambrian Ouarzazate Group formations and in the Cambrian–Ordovician rocks. In accordance with the values of sulfates precipitated in Permian–Triassic seawater (i.e., +11 to +18‰ $\delta^{34}\text{S}$) [88], all analyzed barite samples had uniform $\delta^{34}\text{S}$ ratios ranging from +10.8 to +15‰ (Figure 9a), except for sample MO-15 (Table 2), which exhibited the highest $\delta^{34}\text{S}$ value of 19.5‰. The distribution of $\delta^{34}\text{S}$ ratios of vein barite in the Ougnat Massif shows no spatial variation. These data are comparable to $\delta^{34}\text{S}$ values of +8.9 to +14.7‰ for vein and karstic barite deposits in the Western Jebilet (Meseta) [19], as well as $\delta^{34}\text{S}$ values ranging from +11 to +13.4‰ for vein and karstic barite deposits in the High Moulouya [17]. Furthermore, in the High Atlas, the Bou Dher deposit (Pb–Zn–Ba) is hosted within the Lower and Middle Triassic terrains showing $\delta^{34}\text{S}$ values ranging from 17.2 to 20.4‰ [89]. Further north in the Rif belt, the Jebel Ouichane barite deposit is embedded within iron-bearing skarns, developed within Jurassic–Cretaceous limestones and showing $\delta^{34}\text{S}$ values of around +16.39‰ [90]. However, these values significantly contrast with the documented values for the Cambrian barite deposit in Bouznika (Meseta) ($\delta^{34}\text{S} = +31$ to +38‰) [91].

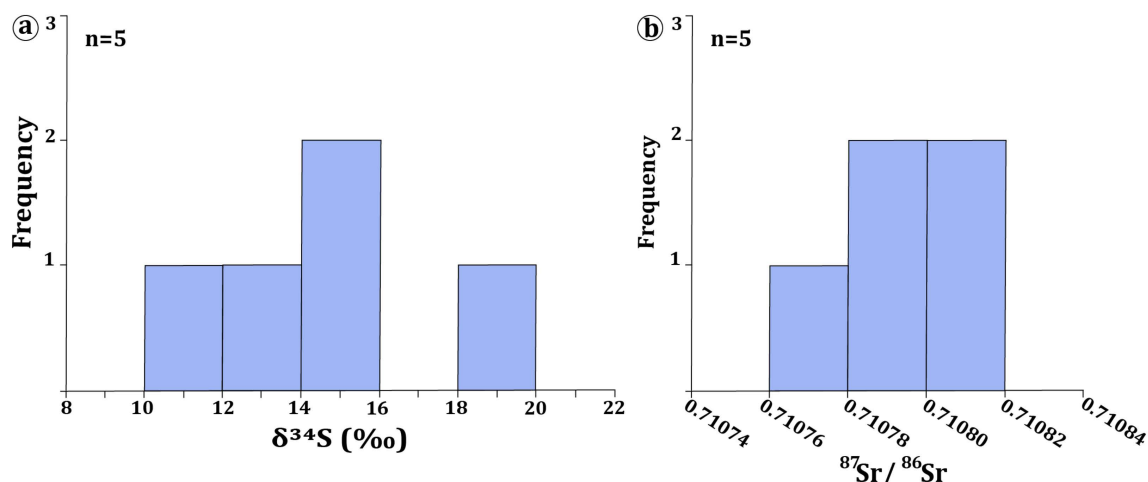


Figure 9. (a) Frequency diagram showing the distribution of $\delta^{34}\text{S}$ values in barite from barite \pm sulfides hydrothermal vein system of Ougnat, eastern Anti-Atlas. (b) Frequency diagram summarizing the distribution of $^{87}\text{Sr}/^{86}\text{Sr}$ ratios for barite from the barite \pm sulfides hydrothermal vein system.

Table 2. Radiogenic and stable isotope of selected barite samples from the important barite veins of the Ougnat Massif.

Sl. No	Sample No	Latitude (N)	Longitude (W)	Mineral	$\delta^{34}\text{S}$ (‰ vs. CDT)	$^{87}\text{Sr}/^{86}\text{Sr}$
1	MO-3	31°21'10.63"	5°5'28.57"	White barite	12.5	0.710787
2	MO-7	31°22'11.98"	5°2'19.11"	Grey barite	14.3	0.710810
3	MO-9	31°29'14.08"	4°58'13.10"	Grey barite	15	0.710772
4	MO-13	31°33'33.92"	4°50'30.84"	Pink barite	10.8	0.710816
5	MO-15	31°31'30.14"	4°39'21.10"	White barite	19.5	0.710793

5.3. Strontium Isotopes

Isotopic analyses of strontium were performed on (5) samples of barite originating from veins in different directions. The results of these analyses are summarized in Table 2 and presented in the frequency histogram in Figure 9b. The $^{87}\text{Sr}/^{86}\text{Sr}$ ratios of the studied barite samples ranged from 0.710772 to 0.710816. In the frequency histogram (Figure 9b), a single group of Sr isotopic ratios can be distinguished. The $^{87}\text{Sr}/^{86}\text{Sr}$ ratios remained consistently high and comprise all barite types located in veins of varying orientations, regardless of the presence of sulfides.

5.4. Fluid Inclusions

This study focused on fluid inclusions (FI) in barite samples of various colors and textures from the main vein systems of the Ougnat Massif. The samples show a wide range of FI. The identification of primary (P) and secondary (S) FI follows the guidelines of [92,93]. Most of the inclusions analyzed appear to be streaks of various shapes, including oval, rounded, or elongated, distributed either within growth zones (PFI) or along secondary fractures and cracks that intersect primary growth zones (SFI) (Figure 10b,c,e and Figure 10a,c,d respectively). In addition, a few isolated and scattered inclusions of tabular, elongated, or regular shapes were also identified. At room temperature, most FI exist in a two-phase state containing both liquid and vapor phases. The liquid phase makes up the bulk of the composition, accounting for 70–80%, while maintaining a constant vapor/liquid ratio. In some FI, solids may be present, resulting in a three-phase system of liquid, vapor, and solid. Note that CO_2 was not detected at room temperature or during cooling.

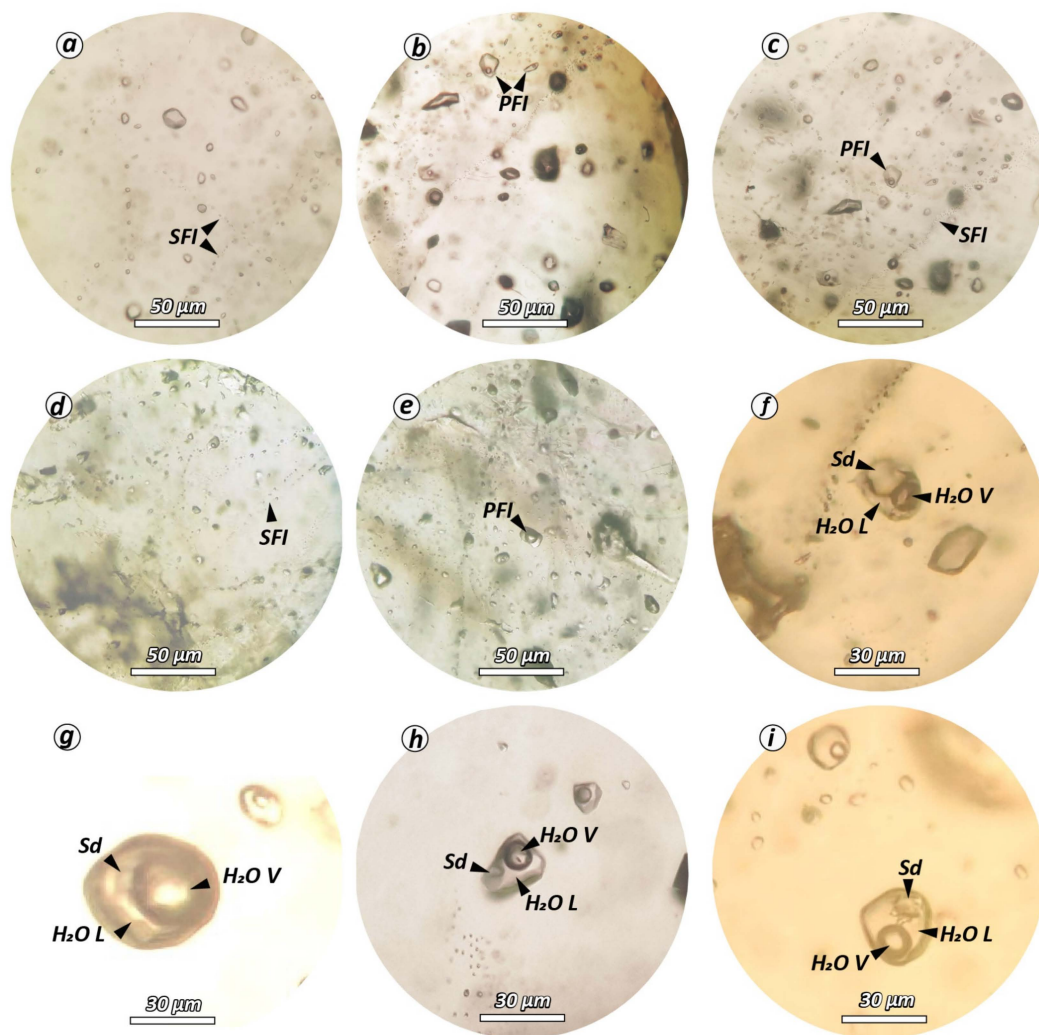


Figure 10. Photomicrographs of the different FI studied in the various barite from Ougnat. These photographs were taken at a temperature of +22 °C under transmitted polarized light. (a,c,d) Secondary FI are aligned along fractures. (b,c,e) Primary FI, comprising approximately 85%, occurs in clusters parallel to growth zones. These inclusions are rich in liquid. (f–i) Primary FI containing a solid body inside. PFI: primary fluid inclusions, SFI: secondary fluid inclusions, Sd: solid, H₂O L: H₂O Liquid and H₂O V: H₂O vapor.

Some samples exhibited FI composed exclusively of liquid (monophasic), but they were rare. FI that are biphasic display distinct petrographic characteristics because of the distinct physical properties of barite. Most FI are clear, angular, and small (5–15 μm), but some are larger (up to 35 μm) and have a more uniform, darker appearance. Please refer to Figure 10f. These FI have liquid-to-vapor ratios ranging from 10 to 20% gas volume (Lw) and sometimes 60 to 80% (Vw), and often occur as isolated clusters along streaks. In most barite samples, the ratios between liquid and vapor within a particular range or trail can vary. Triphasic inclusions composed of liquid, vapor, and solid phases are relatively infrequent, and the solid phase is identified as halite (Ls). These inclusions are typically sub-spherical in shape and vary in size from 5–30 μm. The gas volume ranges from 10 to 20%, whereas the solid percentage occupies 4 to 12% of the total inclusion volume. Microthermometric measurements were carried out on inclusions that became homogenized by the disappearance of the vapor bubbles. In this study, we identified the initial (T_e) and final (T_{m_ice}) fusion temperatures of ice, along with the final fusion temperature of the solid phase (halite; T_{m_Solid}) (Figure 10f–i) and the homogenization temperature (T_h) for 50 inclusions (Lw, Vw and Ls) (Figure 11c). The temperature of the

last solid phase fusion was recorded for 9 of these inclusions (Ls). We used the halite dissolution temperature based on the [94] method to calculate the fluid salinity (Figure 11d). The analytical data are presented in Table 3 and Figure 11.

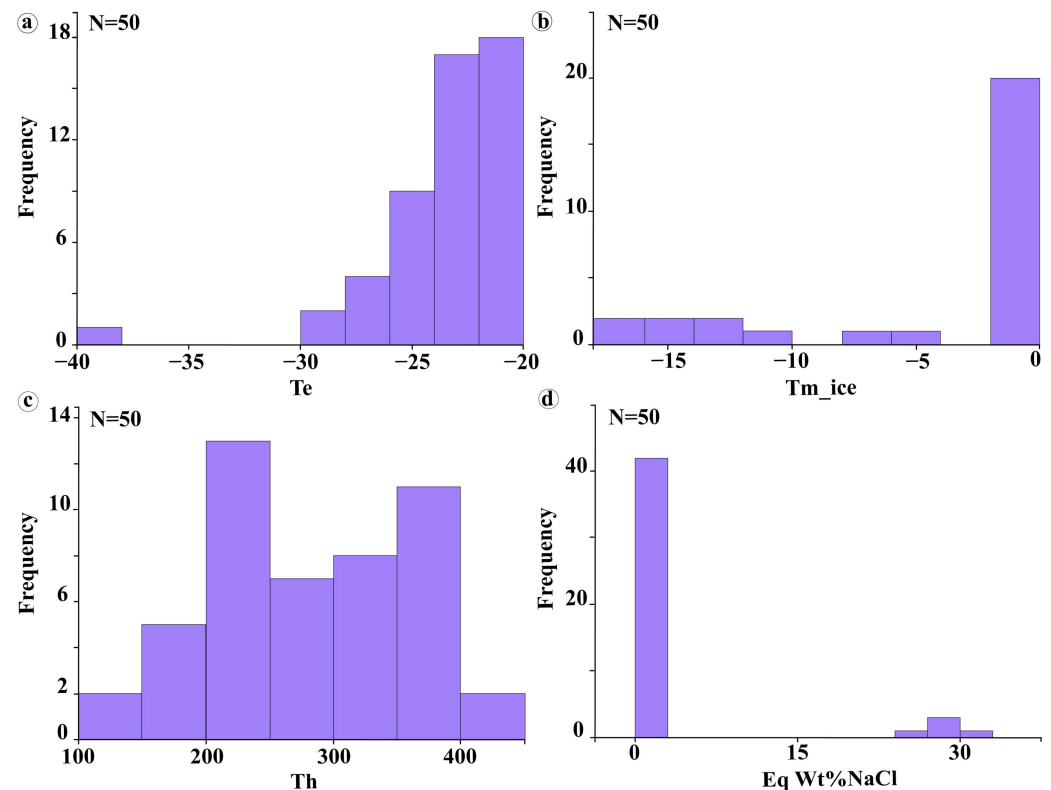


Figure 11. Frequency diagrams summarizing the temperature distribution of FIs trapped in barite. (a) Frequency vs. start ice melting temperature (Te). (b) Frequency vs. final ice melting temperature (Tm_ice). (c) Frequency vs. homogenization temperature (Th). (d) Frequency vs. fluid salinity (EqWt%NaCl).

Table 3. Summary of microthermometric data of fluid inclusions hosted in barite from the Ougnat Massif.

Measurement No.	Barite Studied	FI Type	RV%	Te	Tm_Ice	Tm_Solid	Th	% NaCl
1	8/3.	Lw	10%	−21.6	−0.1		208.3	0.18
2	6/4.	Lw	10%	−21.5	0		216.2	0
3	1/1.	Lw	10%	−22.1	−0.1		180.1	0.18
4	2/2.	Lw	20%	−22.1	0		183.2	0
5	7/4.	Lw	10%	−22.1	0		183.2	0
6	8/1.	Lw	15%	−21.8	0		185.3	0
7	14/2.	Lw	10%	−22.3	−0.3		188.6	0.35
8	10/2.	Lw	10%	−24.5	0		200.4	0
9	12/3.	Lw	10%	−22.4	0		201.7	0
10	13/4.	Lw	10%	−22.6	−0.1		227.6	0.18
11	1/2.	Lw	12%	−21.1	0		229.3	0
12	10/3.	Lw	10%	−22.8	0		234.1	0
13	12/4.	Lw	20%	−23.1	−1.4		244.6	0.7
14	7/2.	Lw	12%	−21.9	0		245.2	0
15	13/3.	Lw	15%	−22.2	−0.1		246.3	0.18
16	16/5.	Lw	15%	−22.1	0		246.3	0
17	6/3.	Lw	10%	−21.1	−0.1		255.4	0.18
18	16/4.	Lw	15%	−21.3	−0.3		263.2	0.35
19	16/6.	Lw	15%	−22.1	0		263.2	0
20	5/1.	Lw	15%	−22.2	−0.1		285.3	0.18

Table 3. Cont.

Measurement No.	Barite Studied	FI Type	RV%	Te	Tm_Ice	Tm_Solid	Th	% NaCl
21	8/4.	Lw	10%	−22.2	−0.9		286.3	0.7
22	16/3.	Lw	10%	−24.6	0		296.9	0
23	7/3.	Lw	10%	−22	0		321.4	0
24	7/1.	Lw	10%	−21.1	0		329.3	0
25	6/5.	Lw	10%	−21.5	0		328.9	0
26	2/1.	Lw	15%	−21.4	−0.2		331.2	0.35
27	11/1.	Lw	15%	−21.3	0		335.5	0
27	11/1.	Lw	15%	−21.3	0		335.5	0
28	6/7.	Lw	10%	−22.1	−0.2		347.8	0.35
29	8/2.	Lw	15%	−21.9	0		347.8	0
30	11/2.	Lw	10%	−21.5	0		348.7	0
31	2/3.	Lw	10%	−21.3	0		352.3	0
32	16/2.	Lw	12%	−24.6	−0.1		355.4	0.18
33	6/6.	Lw	10%	−22.1	−0.1		359.7	0.18
34	8/5.	Vw	75%	−24.6	−0.2		389.8	0.35
35	8/6.	Vw	70%	−21.5	−0.3		364.6	0.35
36	8/7.	Vw	65%	−26.4	−0.4		375.3	0
37	11/3.	Vw	70%	−25.2	0		368.1	0
38	11/4.	Vw	60%	−24.8	0		425.3	0
39	12/1.	Vw	70%	−28.3	−0.2		372.3	0.35
40	12/2.	Vw	65%	−26.4	−0.1		405.6	0.18
41	14/1.	Vw	80%	−25.3	−0.1		364.8	0.18
42	6/1.	Ls	10%	−26.5	−12.6	256.5	392.5	29.5
43	6/2.	Ls	10%	−24.2	−10.5	238.5	368.4	27.5
44	7/5.	Ls	12%	−22.6	−16.2	285.2	412.9	30.5
45	10/5.	Ls	12%	−25.1	−14.4	280.1	345.2	30
46	10/6.	Ls	10%	−23.8	−6.2	228.6	336.3	25.3
47	13/1.	Ls	15%	−39.1	−14.5	251.8	328.8	29.2
48	13/2.	Ls	20%	−27.7	−13.6	202.5	329.5	27
49	16/1.	Ls	15%	−28.2	−5.6	293.6	358.6	31.2
50	16/7.	Ls	15%	−21.6	−17.3	288.7	388.2	30.3

The liquid biphasic fluids (Ls) had the highest representation and demonstrated Te values ranging from −21.6 to −39.1 °C and TfG values from −5.6 to −17.3, which align with NaCl contents ranging from 25.3 to 31.2% NaCl. Additionally, Th values varied between 328.8 and 412.9 °C. In the case of biphasic vapor fluids, Te values ranged from −21.5 to −28.3 while TfG values ranged from 0 to −0.4 which correlates to NaCl contents of 0 to 0.35%. Th values ranged from 364.6 to 425.3 °C. The higher homogenization temperatures observed in barite were likely a result of re-equilibration after trapping, including neck shrinkage or expansion, which may be due to variations in the FI H₂O liquid/vapor ratio as reported by [19].

Three-phase fluid inclusions (Ls) can provide microthermometric data across a wide temperature range. The ice melting temperatures had an initial value of −39.1 °C to −21.6 °C, while the final melting temperatures (Tm_ice) range from −6.2 °C to −17.3 °C (Figure 11b). These higher temperatures indicated Na⁺ as the dominant cation in this inclusion but did not eliminate the possibility of smaller amounts of other cations, such as Ca⁺⁺ [95]. A decrease in the initial melting temperature of ice is generally observed with increasing salinity. This suggests a preference for Ca⁺⁺ as the primary cation in fluid inclusions [96]. Salinities of three-phase inclusions ranged from 25.3 to 31.2% wt NaCl equivalence, with halite dissolution temperatures varying between 202.5 and 293.6 °C. Homogenization temperatures for vapor–liquid–solid inclusions in the liquid phase ranged from 328.8 to 412.9 °C.

6. Discussion

6.1. Sources of S, Sr, and Ba in the Barite Deposits

The S and Sr isotopic ratios are widely used to determine the sources of mineralizing fluids [19,97–101]. The isotopic compositions of S in the barites from the study area (10.8 to 19.5‰) mainly fell within the range of $\delta^{34}\text{S}$ values of Late Triassic to Jurassic seawater (11 to 14‰) [15,17,19,91,102]. This suggests that a portion of the sulfide (SO_2^-) in barite originates from sulfate present in seawater (Figure 9a). This range of $\delta^{34}\text{S}$ values also roughly corresponds to hydrothermal barites (with $\delta^{34}\text{S}$ values in the range of 1.5 to 20.0‰) [103]. The $\delta^{34}\text{S}$ range of the barites in the Ougnat Massif resembles those previously studied in the Jbelets and High Moulouya Massifs [17,19].

Barite is found in different ore formation contexts associated with various types of deposits. In Sedex-type deposits, barite typically exhibits stratification with $\delta^{34}\text{S}$ values ranging from 19.7 to 33.6‰ and 32.3 to 41.6‰ [104]. Massive sulfide volcanic deposits display $\delta^{34}\text{S}$ values ranging from 13.8 to 22.5‰ [105], while those associated with orogenic gold and Carlin-type deposits show variable $\delta^{34}\text{S}$ values. Early-formed barite is characterized by $\delta^{34}\text{S}$ values ranging from 25.9 to 47.1‰, whereas late-formed barite exhibits $\delta^{34}\text{S}$ values between 14.5 and 39.4‰ [106]. In Mississippi valley type (MVT) deposits, where sulfur originates from an evaporite source, $\delta^{34}\text{S}$ values range from 9.6 to 15‰ [102,107,108]. Our $\delta^{34}\text{S}$ data show close similarity to MVT barite deposits. Furthermore, the vein-like structures of the Ougnat barite show no sedimentary structure but exhibit epigenetic hydrothermal characteristics (Figure 12). These features are essential characteristics of tectonically controlled vein-type barite mineralization [109–111].

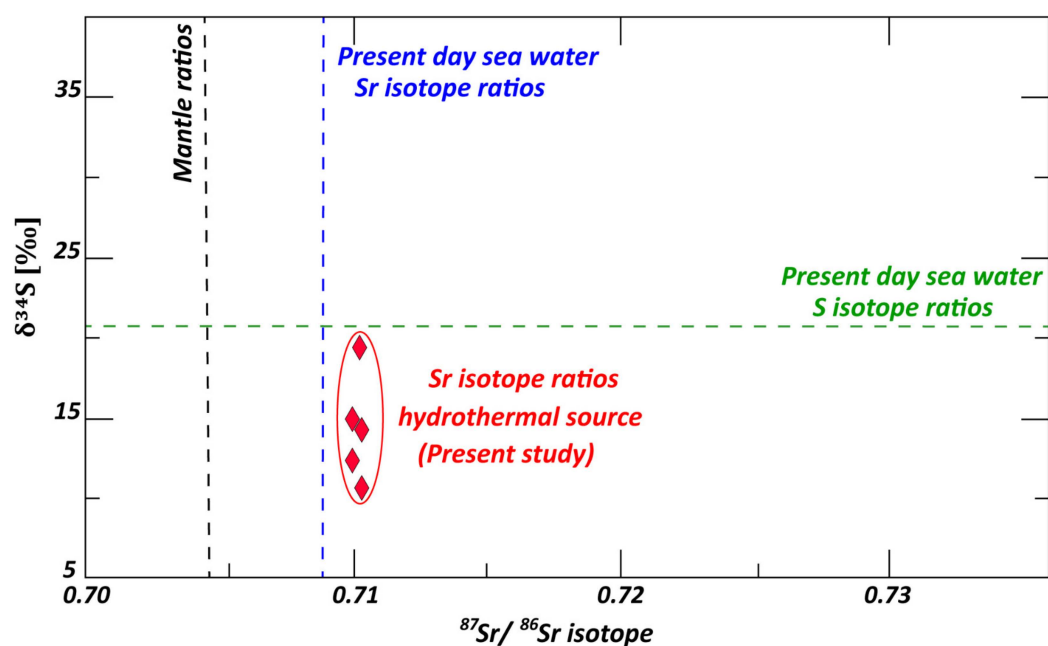


Figure 12. Plot showing $\delta^{34}\text{S}$ and $^{87}\text{Sr}/^{86}\text{Sr}$ isotope values for barite samples showing source (after [112–114]). Dotted lines explain present-day seawater Sr and S isotope ratios.

According to the studies conducted by [115] and [116], the isotopic composition of strontium in barite reveals the isotopic composition of the fluid involved in the hydrothermal process (Figure 12). The $^{87}\text{Sr}/^{86}\text{Sr}$ ratio fractionates either below 400 °C or during hydrothermal crystallization or dissolution. Additionally, the parent of ^{87}Sr , namely ^{87}Rb , generally does not incorporate into the crystal lattice of barite [116]; thus, the strontium composition of barite remains relatively constant over time. In the Ougnat Massif, measurements revealed a moderate to high $^{87}\text{Sr}/^{86}\text{Sr}$ ratio (ranging from 0.710772 to 0.710816) (Figure 9b). These values lie between the radiogenic isotopic compositions of strontium in the mineralization deposit by hydrothermal solutions interacting with crustal brine [114]

and the non-radiogenic isotopic signature of seawater from the Triassic to Jurassic periods [19]. This type of deposit resembles those observed in cratonic rifts [117]. Similar strontium isotopic compositions have been found in other deposits [10,11], supporting the concept of a common source for mineralizing fluids. Furthermore, Ref. [103] proposed that elevated $^{87}\text{Sr}/^{86}\text{Sr}$ isotopic ratios (>0.707) are characteristic of crustal brines derived from the basement, while lower $^{87}\text{Sr}/^{86}\text{Sr}$ ratios (<0.707) correspond to fluids derived from sedimentary cover. In summary, isotopic analyses of strontium in barite provide valuable information on the origin and evolution of fluids involved in hydrothermal processes, shedding light on the geological conditions that led to these deposits.

The main minerals responsible for releasing strontium into fluids circulating in crystalline rocks such as granodiorite, rhyolite, dacite, and andesite are plagioclase, potassium feldspars, and mica. These minerals produce Sr with high $^{87}\text{Sr}/^{86}\text{Sr}$ ratios [118–120]. The relatively radiogenic Sr isotopic compositions of many barites indicate that potassium feldspars and micas from these rocks are the most probable sources of Sr. Therefore, these two minerals are also the most probable sources of Ba for barite mineralization. Furthermore, geochemical analyses conducted by [33], have shown that volcanic facies in the Ouarzazate group (rhyolites, andesites, and ignimbrites) in the Ougnat Massif are rich in Ba (713 to 2069 ppm) and slightly in Sr (140 to 399 ppm). These concentrations are sufficiently high to suggest that these facies could have been a potential source of Ba for the hydrothermal alteration-induced barite mineralization in the Ougnat Massif, involving the alteration of feldspars and micas.

6.2. Fluid Mixing Model

The data projection of PFL: In barite growth zones, Vw and Ls are present along with SFL that intersect the PFL planes. As shown in the diagram (Figure 13a), the salinity-temperature homogenization discrimination suggests fluid homogenization at (i) moderately high temperatures and high salinity during the initial phase (Vw and Ls), followed by (ii) moderate temperatures and low salinity during later phases (Lw). The range of salinity levels found in Ls-type fluid inclusions in the examined barites indicates a significant mixture of a colder, less salty fluid composed of seawater, meteoric water, and hydrothermal fluids within the system (Figure 13b). The analysis suggests that fluid immiscibility occurred before entrapment as a result of high salinity and homogenization temperature [93,99]. The simultaneous existence of saline and less saline fluid inclusions was likely during the ultimate stage of barite crystallization [92]. The decrease in salinity of the fluid occurred due to the formation of sulfides, including galena and chalcopyrite, through combination with seawater during temperatures ranging from 360 to 180 °C (Figure 13b).

Microthermometry has enabled the identification of two types of hydrothermal fluids, L1 and L2, associated with barite in the Ougnat region. L1 and L2 originate from the boiling of an initial fluid (Lin H; Figure 13a), assumed to contain about 15% NaCl eq., and estimated to have a density and temperature between 425 and 365 °C (Figure 13a), corresponding to a pressure between 346 and 187 bar and a depth between 3.45 and 1.86 km. Fluid L1, which is represented as Lw, has an average temperature of 390 °C, a salt equivalence of 0.18%, an average pressure of 246 bar at a depth of 2.45 km, and a density of 0.30. Fluid L2, represented as Ls, has an average temperature of approximately 362 °C, which represents a salt equivalence of 25.89%, resulting in a density near 0.90. The pressure is around 182 bar, corresponding to a depth of around 1.81 km. This situation is similar to many hydrothermal barite ± sulfide deposits formed along faults between the basement and cover rocks worldwide [17,92,99,103,109,121]. We can conclude that the deposition and precipitation of barite mineralization is the result of mixing two or more fluids. One of these fluids originates from depth and has leached the granodiorites as well as the volcanic-sedimentary complex of the Ouarzazate group, thereby contributing to the hydrothermal system by mainly supplying Ba, radiogenic Sr, as well as a portion of dissolved Ca, Na, and S. The second fluid is of surface origin and corresponds to Late Triassic to Jurassic seawater.

This low-temperature fluid was enriched in SO_4^{-2} and Na and depleted in Ca compared to the upwelling hot fluid.

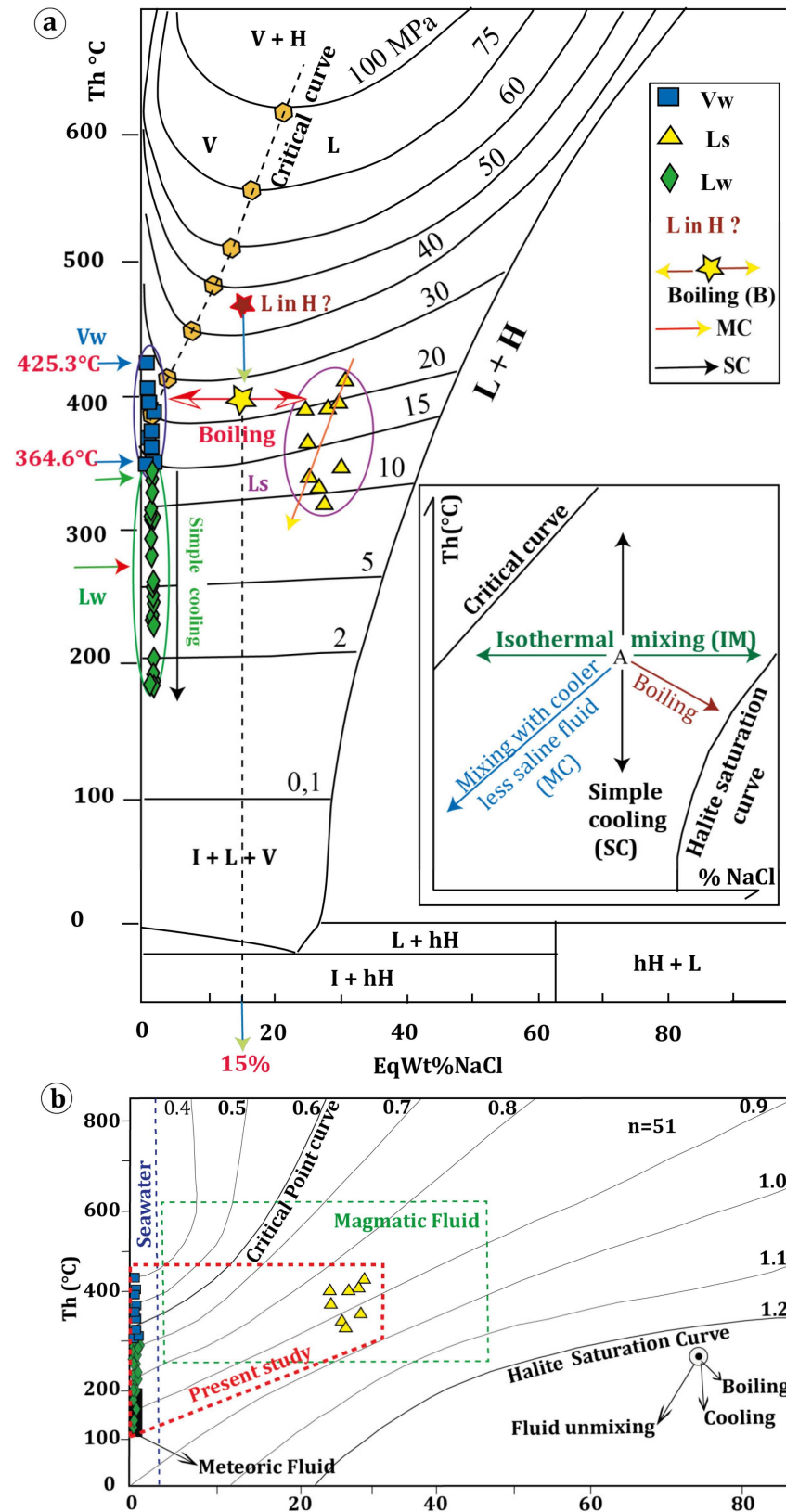


Figure 13. Homogenization temperature vs. salinity of PFI trapped in different generations of barite from the hydrothermal barite vein system of the Ougnat Massif adopted from [122] (a) and [123] (b). Vw, Ls, and Lw: FI types, L in H?: initial fluid, V: Vapor, H: Halite, L: Liquid, hH: Hydrohalite and I: Ice.

6.3. Barite Ore Genesis

Based on our field observations, structural studies, fluid inclusions, and sulfur with strontium isotope analyses, we propose a metallogenic model to explain the setting process of the barite mineralization in the Ougnat Massif (Figure 14). Hydrothermal alteration resulted in the hydration of potassium feldspars present in the granodiorites and magmatic formations of the Ouarzazate group (rhyolites, dacites, etc.), leading to the dissolution of alkalis, silica, and barium. Barium was gradually released from potassium feldspars and micas as temperatures decreased, thus entering the mineralizing fluid. Through high hydrostatic pressure, barium-rich deep fluids were able to ascend to shallow levels along opening faults. Concurrently, infiltration of late Triassic to Jurassic seawater introduced sulfates (SO_4^{-2}), causing the precipitation of barite along strike-slip/normal fault systems (Figure 14). This is further supported by sulfur isotope ($\delta^{34}\text{S}$) data and $^{87}\text{Sr}/^{86}\text{Sr}$ isotopes. Boiling and fluid mixing resulted in the separation of less saline vapors from the mineralized fluid containing Ba. Increasing concentrations of Ba^{+2} also reduced the solubility of barite in the solution, promoting its precipitation.

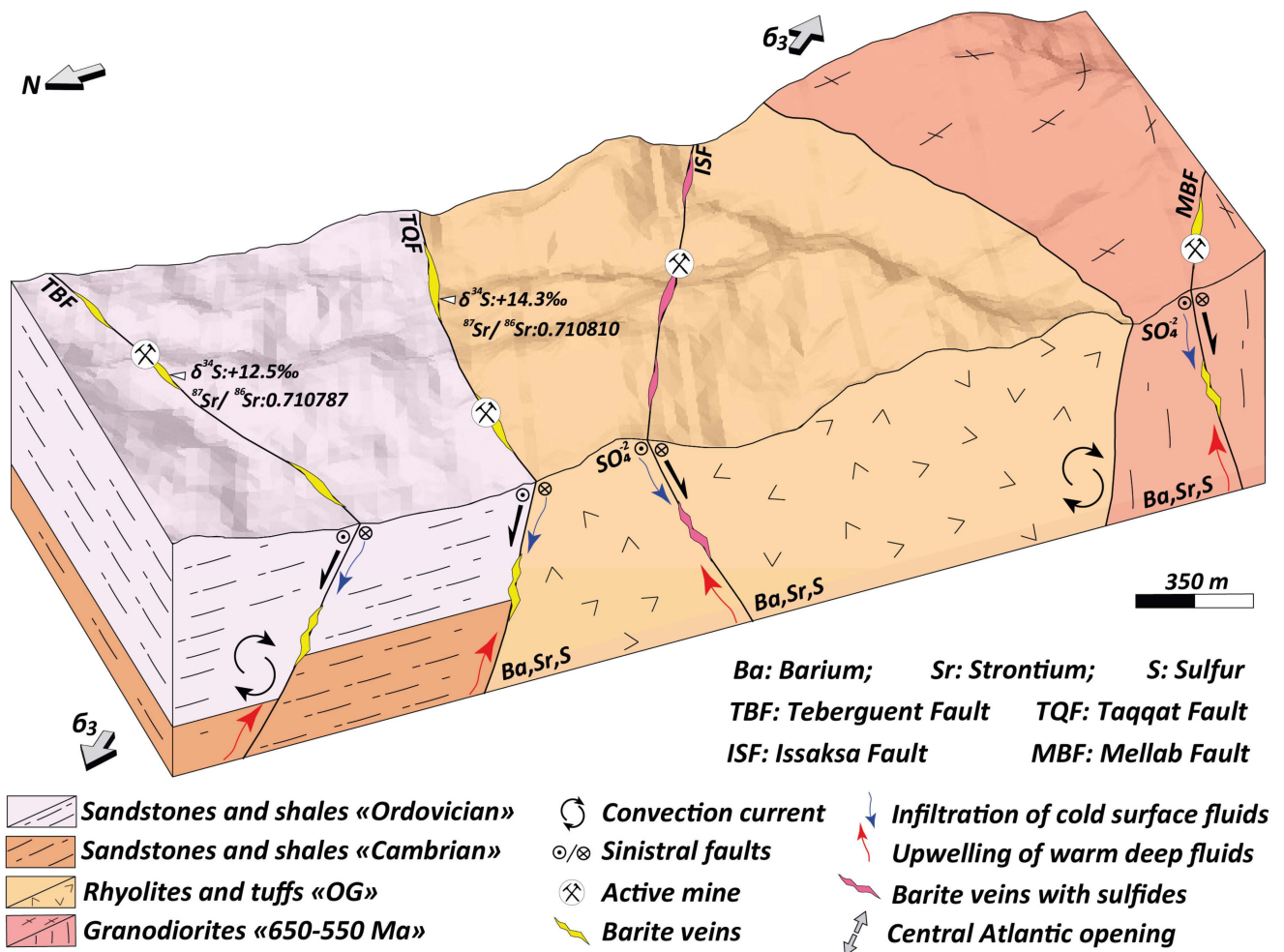


Figure 14. Genetic model illustrating the formation of barite mineralization through the mixing of multi-component fluids and the development of mineralized veins.

During the fluid mixing process, barite precipitation was predominant in the study area. Barite veins without sulfides form when fluids lack a reducing agent [99]. Furthermore, certain conditions favor high salinity (8–20.66% NaCl eq.) in a neutral environment. However, the formation of sulfur-bearing barite likely happens when the fluids are mixed with seawater. To achieve this, reducing agents such as methane need to be added to the mixing of aqueous fluids [99,123]. Veins of sulfur-bearing and non-sulfur-bearing

barite formed in spatial and temporal proximity. Structural analyses and Sr-S isotope studies of barite have yielded valuable insights, firmly establishing that the barite within the Ougnat Massif is indeed of tectonic origin, specifically formed through hydrothermal vein processes.

6.4. Geodynamic Context

Based on structural evidence [18] and strontium-sulfur isotopes here studied here, it is apparent that the formation of barite mineralization in the Ougnat Massif is intimately tied to the geologic events related to the rifting and opening of the Central Atlantic. The opening of the Central Atlantic Ocean led to multiple phases of extension, uplift, and subsidence of the continental crust, which directly influenced the geology and metallogeny of the passive margin of North Africa and North America. During the first phase of the central Atlantic opening (Anisian–Hettangian), the formation of large subsiding continental basins was followed by thermal uplift of the rift margins during the second phase of rifting [124]. This thermal uplift of the rift margins can be attributed to the formation of an asthenospheric diapir, which altered the distribution of isotherms and locally induced the formation of small-scale convection cells in the continental crust [124]. These convection cells could have caused the heating and circulation of deep basic fluids. These hot fluids would have migrated to shallower levels of the crust, where they would have mixed with colder, less saline fluids from the surface, creating an environment particularly favorable for barite precipitation. This scenario, according to Emery et al. [125], is supported by the fact that the late mineralization stage approximately coincides with the thermal subsidence of the African passive margin and the onset of seafloor spreading.

7. Conclusions

The isotopic data of S and Sr, along with the microthermometry of fluid inclusions in barite from the Ougnat Massif, allow us to understand the origin of the fluids responsible for mineralization. These data support a genetic model based on the mixing of two types of fluids with different thermal and geochemical properties. The sulfur in barite is derived from both late Triassic to Jurassic seawater and leaching from granodiorites and the volcano-sedimentary complex of the Precambrian Ouarzazate group, which contribute dissolved sulfur to the hydrothermal system. Sr and Ba are mainly released by minerals such as plagioclase, potassium feldspar, and mica found in crystalline rocks such as granodiorites, rhyolites, dacites, and andesites. Data on fluid inclusions indicate that the fluids involved in ore formation are the result of the mixing of two or more fluids. A deep, hot fluid with an average temperature of 368 °C has leached the granodiorites and volcanic-sedimentary complex of the Ouarzazate Group. This fluid has provided the hydrothermal system with most of the Ba, radiogenic Sr, and some of the dissolved S. A second, shallow fluid with an average temperature of 242 °C was derived from Late Triassic to Jurassic seawater. A dynamic two-component mixing model between deep, saline fluids and shallow fluids satisfactorily reproduced the S and Sr isotopic data of barite deposits. The genetic analogy between Paleozoic and Mesozoic barite deposits in Spain, France, Germany [126–131], and the Ougnat Massif suggests that they formed in similar tectonic context resulting from the rifting and opening of the central Atlantic, and they are part of a single large-scale mineralization event encompassing North Africa and Central and Western Europe.

Author Contributions: Conceptualization, S.S. and A.A.; methodology, S.S.; software, S.S., A.B., O.L. and A.A.; validation, A.B., B.M., L.B. and A.E.; formal analysis, S.S., A.A. and A.N.B.; resources, A.B.; data curation, S.S.; writing—original draft preparation, S.S.; writing—review and editing, S.S., A.A. and A.N.B.; visualization, A.A.; supervision, S.S.; project administration, S.S. All authors have read and agreed to the published version of the manuscript.

Funding: This research received no external funding.

Data Availability Statement: Data are contained within the article.

Acknowledgments: This work is a part of Samir Samaoui’s doctoral dissertation which be submitted to the Department of Geology, Faculty of Sciences Dher Al Mahraz, Sidi Mohamed Ben Abdellah University of Fez.

Conflicts of Interest: The authors declare no conflicts of interest.

References

- Clark, S.H.B.; Poole, F.G.; Wang, Z. Comparison of Some Sediment-Hosted, Stratiform Barite Deposits in China, the United States, and India. *Ore Geol. Rev.* **2004**, *24*, 85–101. [[CrossRef](#)]
- Johnson, C.A.; Dumoulin, J.A.; Burruss, R.A.; Slack, J.F. Depositional Conditions for the Kuna Formation, Red Dog Zn-Pb-Ag-Barite District, Alaska, Inferred from Isotopic and Chemical Proxies. *Econ. Geol.* **2015**, *110*, 1143–1156. [[CrossRef](#)]
- Li, W.Y.; Yu, H.Y. *Barite Deposit in China*; Geological Publishing House: Beijing, China, 1991.
- Li, Y.; Zou, H.; Said, N.; Liu, H. A New Classification of Barite Deposits in China. *Ore Energy Resour. Geol.* **2023**, *14*, 100019. [[CrossRef](#)]
- Tas Ozdogan, A.; Uras, Y.; Oner, F. Geochemistry of the Barite Deposits near Adana-Feke Area (Eastern Taurides). *Russ. Geol. Geophys.* **2017**, *58*, 1349–1365. [[CrossRef](#)]
- Tombros, S.F.; Seymour, K.S.; Williams-Jones, A.E.; Zhai, D.; Liu, J. Origin of a Barite-Sulfide Ore Deposit in the Mykonos Intrusion, Cyclades: Trace Element, Isotopic, Fluid Inclusion and Raman Spectroscopy Evidence. *Ore Geol. Rev.* **2015**, *67*, 139–157. [[CrossRef](#)]
- Wu, S.; Liu, J.; Zhai, D. Factors Controlling Precipitation of Barite and Witherite and Genesis of the Ankang–Xunyang Barium Deposits, Shaanxi, China. *Acta Geol. Sin. Engl. Ed.* **2015**, *89*, 836–851. [[CrossRef](#)]
- Xu, L.; Lehmann, B.; Mao, J.; Zheng, W.; Ye, H.; Li, H. Strontium, Sulfur, Carbon, and Oxygen Isotope Geochemistry of the Early Cambrian Strata-Bound Barite and Witherite Deposits of the Qinling-Daba Region, Northern Margin of the Yangtze Craton, China. *Econ. Geol.* **2016**, *111*, 695–718. [[CrossRef](#)]
- Zhou, C.; Bao, H.; Peng, Y.; Yuan, X. Timing the Deposition of 17O-Depleted Barite at the Aftermath of Nantuo Glacial Meltdown in South China. *Geology* **2010**, *38*, 903–906. [[CrossRef](#)]
- Zou, H.; Fang, Y.; Zhang, S.T.; Zhang, Q. The Source of Fengjia and Langxi Barite–Fluorite Deposits in Southeastern Sichuan, China: Evidence from Rare Earth Elements and S, Sr, and Sm–Nd Isotopic Data. *Geol. J.* **2017**, *52*, 470–488. [[CrossRef](#)]
- Zou, H.; Zhang, S.T.; Chen, A.-q.; Fang, Y.; Zeng, Z.F. Hydrothermal Fluid Sources of the Fengjia Barite–Fluorite Deposit in Southeast Sichuan, China: Evidence from Fluid Inclusions and Hydrogen and Oxygen Isotopes. *Resour. Geol.* **2016**, *66*, 24–36. [[CrossRef](#)]
- Azza, A.; Makkoudi, D. Cadre Structural Des Minéralisations Plombo-Barytiques de Tafilalet. *Mines Géologie Et Énergie* **1996**, *55*, 175–184.
- Bouabdellah, M.; Margoum, D. Geology, Fluid Inclusions, and Geochemistry of the Aouli Sulphide ± Fluorite ± Barite Vein Deposit (Upper Moulouya District, Morocco) and Its Relationships to Pangean Rifting and Opening of the Tethys and Central Atlantic Oceans. In *Mineral Deposits of North Africa*; Springer: Cham, Switzerland, 2016; pp. 291–305. [[CrossRef](#)]
- Caia, J.; Huvelin, P. *Géologie Des Gites Minéraux Marocains: Baryum et Strontium*; Editions du Service Géologique du Maroc: Rabat, Morocco, 1980; Volume 276, pp. 271–308.
- El Hnot, H.; Mzahraoui, M. Origine et Mode de Mise En Place de La Barytine Du Gisement de Bou Ouzzal (Meseta Marocaine). *Bull. De L’institut Sci. Rabat* **2005**, *27*, 47–54.
- Marcoux, É.; Jébrak, M. Plumbotectonics of Moroccan Ore Deposits. *BSGF Earth Sci. Bull.* **2021**, *192*, 31. [[CrossRef](#)]
- Margoum, D.; Bouabdellah, M.; Klügel, A.; Banks, D.A.; Castorina, F.; Cuney, M.; Jébrak, M.; Bozkaya, G. Pangea Rifting and Onward Pre-Central Atlantic Opening as the Main Ore-Forming Processes for the Genesis of the Aouli REE-Rich Fluorite-Barite Vein System, Upper Moulouya District, Morocco. *J. Afr. Earth Sci.* **2015**, *108*, 22–39. [[CrossRef](#)]
- Samaoui, S.; Aabi, A.; Nguidi, M.A.; Boushaba, A.; Belkasm, M.; Baidder, L.; Bba, A.N.; Lamrani, O.; Taadid, M.; Zehni, A. Fault-Controlled Barite Veins of the Eastern Anti-Atlas (Ougnat, Morocco), a Far-Field Effect of the Central Atlantic Opening? Structural Analysis and Metallogenic Implications. *J. Afr. Earth Sci.* **2023**, 104970. [[CrossRef](#)]
- Valenza, K.; Moritz, R.; Mouttaqi, A.; Fontignie, D.; Sharp, Z. Vein and Karst Barite Deposits in the Western Jebilet of Morocco: Fluid Inclusion and Isotope (S, O, Sr) Evidence for Regional Fluid Related to Central Atlantic Rifting. *Econ. Geol.* **2000**, *95*, 587–606. [[CrossRef](#)]
- Wafik, A.; Essaifi, A.; Admou, H.; Mouttaqi, A. The Jbel Irhoud Barite Deposit (Western Jebilet). In *Nouveaux Guides Géologiques et Minières du Maroc*; Editions du Service Géologique du Maroc: Rabat, Morocco, 2011; Volume 9, pp. 199–203.
- Yaagoub, D.; Hinaje, S.; El Fartati, M.; Gharmane, Y. Analysis of Tectonic Fracturing in the Mibladen Ore Deposit (Upper Moulouya, Morocco) and Its Impact on the Pb–Ba Mineralization Emplacement. *Rend. Lincei* **2021**, *32*, 325–342. [[CrossRef](#)]
- Azza, A. Les Minéralisations Barytiques Du Maroc. *Chron. De La Rech. Minière* **1998**, 531–532, 109–116.
- Castorina, F.; Masi, U.; Padalino, G.; Palomba, M. Trace-Element and Sr–Nd Isotopic Evidence for the Origin of the Sardinian Fluorite Mineralization (Italy). *Appl. Geochem.* **2008**, *23*, 2906–2921. [[CrossRef](#)]
- Cherai, M.; Rddad, L.; Talbi, F.; Walter, B.F. Trace-Element Geochemistry and S–O Isotopes in the Fluorite-Barite Mineralization of Merguechoum, Moroccan Eastern Meseta: Insights into Ore Genesis to the Pangea Rifting. *Acta Geochim.* **2023**, *42*, 435–452. [[CrossRef](#)]
- Jaillard, L.; Touray, J.-C.; Badra, L. Les Variations Verticales de La Teneur En Sr de Barytines Filiennes Du Haut-Atlas Occidental, Maroc. Implications Pour La Prospection de Barytine de Qualité Chimique. *C. R. Acad. Sci.* **1989**, *309*, 1007–1012.
- Jaillard, L. Quelques Filons de Barytine En Decrochement et En Extension Dans Le Haut-Atlas Occidental (Maroc). *Chronique de la Recherche Minière* **1985**, *481*, 19–26.

27. Sizaret, S.; Marcoux, E.; Jébrak, M.; Touray, J.C. The Rossignol Fluorite Vein, Chaillac, France: Multiphase Hydrothermal Activity and Intravein Sedimentation. *Econ. Geol.* **2004**, *99*, 1107–1122. [[CrossRef](#)]
28. Schwinn, G.; Markl, G. REE Systematics in Hydrothermal Fluorite. *Chem. Geol.* **2005**, *216*, 225–248. [[CrossRef](#)]
29. Munoz, M.; Premo, W.R.; Courjault-Radé, P. Sm-Nd Dating of Fluorite from the Worldclass Montroc Fluorite Deposit, Southern Massif Central, France. *Miner. Depos. Database* **2005**, *39*, 970–975. [[CrossRef](#)]
30. Piqué, À.; Canals, À.; Grandia, F.; Banks, D.A. Mesozoic Fluorite Veins in NE Spain Record Regional Base Metal-Rich Brine Circulation through Basin and Basement during Extensional Events. *Chem. Geol.* **2008**, *257*, 139–152. [[CrossRef](#)]
31. Sánchez, V.; Vindel, E.; Martín-Crespo, T.; Corbella, M.; Cardellach, E.; Banks, D. Sources and Composition of Fluids Associated with Fluorite Deposits of Asturias (N Spain). *Geofluids* **2009**, *9*, 338–355. [[CrossRef](#)]
32. Dill, H.G.; Hansen, B.T.; Weber, B. REE Contents, REE Minerals and Sm/Nd Isotopes of Granite- and Unconformity-Related Fluorite Mineralization at the Western Edge of the Bohemian Massif: With Special Reference to the Nabburg-Wölsendorf District, SE Germany. *Ore Geol. Rev.* **2011**, *40*, 132–148. [[CrossRef](#)]
33. Abia, E.H.; Nachit, H.; Marignac, C.; Ibhi, A.; Saadi, S.A. The Polymetallic Au-Ag-Bearing Veins of Bou Madine (Jbel Ougnat, Eastern Anti-Atlas, Morocco): Tectonic Control and Evolution of a Neoproterozoic Epithermal Deposit. *J. Afr. Earth Sci.* **2003**, *36*, 251–271. [[CrossRef](#)]
34. Bouabdellah, M.; Levrèse, G. The Bou Madine Polymetallic Ore Deposit, Eastern Anti-Atlas, Morocco: Evolution from Massive Fe–As–Sn to Epithermal Au–Ag–Pb–Zn ± Cu Mineralization in a Neoproterozoic Resurgent Caldera Environment. In *Mineral Deposits of North Africa*; Springer: Cham, Switzerland, 2016; pp. 133–142. [[CrossRef](#)]
35. Dakir, I.; Ahmed, B.; Habiba, A.; Abdessalam, O.; Youssef, A.B. Contribution of Geophysics to the Study of Barite Mineralization in the Paleozoic Formations of Asdaf Tinejdad (Eastern Anti Atlas Morocco). *Econ. Environ. Geol.* **2020**, *53*, 259–269. [[CrossRef](#)]
36. Essalhi, A.; Essalhi, M.; Toummite, A. Environmental Impact of Mining Exploitation: A Case Study of Some Mines of Barite in the Eastern Anti-Atlas of Morocco. *J. Environ. Prot.* **2016**, *07*, 1473–1482. [[CrossRef](#)]
37. Michard, A.; Soulaïmani, A.; Hoepffner, C.; Ouanaimi, H.; Baidder, L.; Rjimati, E.C.; Saddiqi, O. The South-Western Branch of the Variscan Belt: Evidence from Morocco. *Tectonophysics* **2010**, *492*, 1–24. [[CrossRef](#)]
38. Aabi, A.; Hejja, Y.; Nait Bba, A.; Boujamaoui, M.; Baidder, L.; El Azmi, M.; Maacha, L.; Hamzaoui, A. Tectonic Reactivation and Ore-Forming Fault Systems from the West African Craton Margin (Saghro, Anti Atlas, Morocco). *J. Afr. Earth Sci.* **2024**, *211*, 105–182. [[CrossRef](#)]
39. Aabi, A.; Hejja, Y.; Bba, A.N.; Baidder, L.; Fekkak, A.; Bannari, A.; Maacha, L. Polyphase Tectonics, Fault Kinematics and Metallogenic Implications at the Fringe of a Craton (Anti-Atlas, Morocco). *J. Afr. Earth Sci.* **2022**, *196*, 104731. [[CrossRef](#)]
40. Aabi, A.; Baidder, L.; Hejja, Y.; El Azmi, M.; Bba, A.N.; Otmane, K. The Cu-Pb-Zn-Bearing Veins of the Bou Skour Deposit (Eastern Anti-Atlas, Morocco): Structural Control and Tectonic Evolution. *C. R. Geosci.* **2021**, *353*, 81–99. [[CrossRef](#)]
41. Tuduri, J.; Chauvet, A.; Barbanson, L.; Bourdier, J.L.; Labriki, M.; Ennaciri, A.; Badra, L.; Dubois, M.; Ennaciri-Leloix, C.; Sizaret, S.; et al. The Jbel Saghro Au(–Ag, Cu) and Ag–Hg Metallogenic Province: Product of a Long-Lived Ediacaran Tectono-Magmatic Evolution in the Moroccan Anti-Atlas. *Minerals* **2018**, *8*, 592. [[CrossRef](#)]
42. Bouabdellah, M.; Sangster, D.F. Geology, Geochemistry, and Current Genetic Models for Major Mississippi Valley-Type Pb–Zn Deposits of Morocco. In *Mineral Deposits of North Africa*; Springer: Cham, Switzerland, 2016; pp. 463–495. [[CrossRef](#)]
43. Soulaïmani, A.; Michard, A.; Ouanaimi, H.; Baidder, L.; Raddi, Y.; Saddiqi, O.; Rjimati, E.C. Late Ediacaran–Cambrian Structures and Their Reactivation during the Variscan and Alpine Cycles in the Anti-Atlas (Morocco). *J. Afr. Earth Sci.* **2014**, *98*, 94–112. [[CrossRef](#)]
44. Baidder, L.; Michard, A.; Soulaïmani, A.; Fekkak, A.; Eddebbi, A.; Rjimati, E.C.; Raddi, Y. Fold Interference Pattern in Thick-Skinned Tectonics; a Case Study from the External Variscan Belt of Eastern Anti-Atlas, Morocco. *J. Afr. Earth Sci.* **2016**, *119*, 204–225. [[CrossRef](#)]
45. Hejja, Y.; Baidder, L.; Ibouh, H.; Bba, A.N.; Soulaïmani, A.; Gaouzi, A.; Maacha, L. Fractures Distribution and Basement-Cover Interaction in a Polytectonic Domain: A Case Study from the Saghro Massif (Eastern Anti-Atlas, Morocco). *J. Afr. Earth Sci.* **2020**, *162*. [[CrossRef](#)]
46. Aabi, A.; Baidder, L.; Hejja, Y.; Bba, A.N.; El Azmi, M. Reply to Comment by El Ouardi et al. on The Cu-Pb-Zn-Bearing Veins of the Bou Skour Deposit (Eastern Anti-Atlas, Morocco): Structural Control and Tectonic Evolution. *C. R. Geosci.* **2022**, *354*, 125–130. [[CrossRef](#)]
47. de Lamotte, D.F.; Leturmy, P.; Missenard, Y.; Khomsi, S.; Ruiz, G.; Saddiqi, O.; Guillocheau, F.; Michard, A. Mesozoic and Cenozoic Vertical Movements in the Atlas System (Algeria, Morocco, Tunisia): An Overview. *Tectonophysics* **2009**, *475*, 9–28. [[CrossRef](#)]
48. El Hadi, H.; Simancas, J.F.; Martínez-Poyatos, D.; Azor, A.; Tahiri, A.; Montero, P.; Fanning, C.M.; Bea, F.; González-Lodeiro, F. Structural and Geochronological Constraints on the Evolution of the Bou Azzer Neoproterozoic Ophiolite (Anti-Atlas, Morocco). *Precambrian Res.* **2010**, *182*, 1–14. [[CrossRef](#)]
49. Blein, O.; Baudin, T.; Soulaïmani, A.; Cocherie, A.; Chèvremont, P.; Admou, H.; Ouanaimi, H.; Hafid, A.; Razin, P.; Bouabdelli, M.; et al. New Geochemical, Geochronological and Structural Constraints on the Ediacaran Evolution of the South Sirwa, Agadir-Melloul and Iguerda Inliers, Anti-Atlas, Morocco. *J. Afr. Earth Sci.* **2014**, *98*, 47–71. [[CrossRef](#)]
50. Triantafyllou, A.; Berger, J.; Baele, J.M.; Bruguier, O.; Diot, H.; Ennih, N.; Monnier, C.; Plissart, G.; Vandycke, S.; Watlet, A. Intra-Oceanic Arc Growth Driven by Magmatic and Tectonic Processes Recorded in the Neoproterozoic Bougmane Arc Complex (Anti-Atlas, Morocco). *Precambrian Res.* **2018**, *304*, 39–63. [[CrossRef](#)]
51. Triantafyllou, A.; Berger, J.; Baele, J.M.; Diot, H.; Ennih, N.; Plissart, G.; Monnier, C.; Watlet, A.; Bruguier, O.; Spagna, P.; et al. The Tachakoucht–Irirri–Tourtit Arc Complex (Moroccan Anti-Atlas): Neoproterozoic Records of Polyphased Subduction–Accretion Dynamics during the Pan-African Orogeny. *J. Geodyn.* **2016**, *96*, 81–103. [[CrossRef](#)]

52. Ikenne, M.; Souhassou, M.; Cousens, B.; Montero, P.; Bea, F.; Askour, F.; Haissen, F.; Beraaouz, E.H.; Ernst, R.E.; Bajddi, A.; et al. Zircon U–Pb Geochronology and Sm–Nd and Rb–Sr Isotope Systematics of Neoproterozoic Granitoids from Bou Azzer (Anti-Atlas—Morocco): The Obduction Trigger of the Central Anti-Atlas Terrane. *J. Afr. Earth Sci.* **2023**, *202*, 104900. [CrossRef]
53. Fekkak, A.; Pouclet, A.; Benharref, M. The Middle Neoproterozoic Sidi Flah Group (Anti-Atlas, Morocco): Synrift Deposition in a Pan-African Continent/Ocean Transition Zone. *J. Afr. Earth Sci.* **2003**, *37*, 73–87. [CrossRef]
54. Gasquet, D.; Ennih, N.; Liégeois, J.P.; Soulaïmani, A.; Michard, A. The Pan-African Belt. In *Continental Evolution: The Geology of Morocco*; Part of the Book Series: Lecture Notes in Earth Sciences (LNEARTH, Volume 116); Springer: Berlin/Heidelberg, Germany, 2008; pp. 33–64. [CrossRef]
55. Abati, J.; Aghzer, A.M.; Gerdes, A.; Ennih, N. Detrital Zircon Ages of Neoproterozoic Sequences of the Moroccan Anti-Atlas Belt. *Precambrian Res.* **2010**, *181*, 115–128. [CrossRef]
56. Michard, A.; Soulaïmani, A.; Ouanaimi, H.; Raddi, Y.; Aït Brahim, L.; Rjimati, E.C.; Baidder, L.; Saddiqi, O. Saghro Group in the Ougnat Massif (Morocco), an Evidence for a Continuous Cadomian Basin along the Northern West African Craton. In *Proceedings of the Comptes Rendus—Geoscience*; Elsevier Masson SAS: Amsterdam, The Netherlands, 2017; Volume 349, pp. 81–90.
57. Lécolle, M.; Derré, C.; Nerci, K. The Proterozoic Sulphide Alteration Pipe of Sidi Flah and Its Host Series. New Data for the Geotectonic Evolution of the Pan-African Belt in the Eastern Anti-Atlas (Morocco). *Ore Geol. Rev.* **1991**, *6*, 501–536. [CrossRef]
58. Lécolle, M.; Derré, C.; Hadri, M. Les Protolites Des Altérites à Pyrophyllite de l’Ougnat et Leurs Positions Dans l’histoire Du Protérozoïque: Mise à Jour Des Connaissances Géologiques Sur l’Anti-Atlas Oriental. *Afr. Geosci. Rev.* **2003**, *10*, 227–244.
59. Raddi, Y.; Baidder, L.; Tahiri, M.; Michard, A. Variscan Deformation at the Northern Border of the West African Craton, Eastern Anti-Atlas, Morocco: Compression of a Mosaic of Tilted Blocks. *Bulletin de la Société Géologique de France* **2007**, *178*, 343–352. [CrossRef]
60. El-Baghdadi, M.; El-Boukhari, A.; Nadem, S.; Benyoucef, A.; Jouider, A. Typologie Du Zircon Dans Les Granitoïdes de La Boutonnière Précambrienne de Sidi Flah-Bouskour, Saghro, Anti Atlas, Maroc. *J. Afr. Earth Sci.* **2001**, *32*, 635–653. [CrossRef]
61. Mrini, Z.; Rafi, A.; Duthou, J.; Vidal, P. Chronologie Rb–Sr Des Granitoïdes Hercyniens Du Maroc; Consequences | Bulletin de La Société Géologique de France | GeoScienceWorld. Available online: <https://pubs.geoscienceworld.org/sgf/bsgf/article-abstract/163/3/281/122583/Chronologie-Rb-Sr-des-granitoïdes-hercyniens-du> (accessed on 13 June 2023).
62. Cheilletz, A.; Gilles, A.E.; Ae, L.; Gasquet, D.; Rachid, M.; Ae, A.-S.; Zyadi, R.; Archibald, D.A.; Farrar, A.E. The Giant Imiter Silver Deposit: Neoproterozoic Epithermal Mineralization in the Anti-Atlas, Morocco. *Min. Miner Depos* **2002**, *37*, 772–781. [CrossRef]
63. Errami, E.; Bonin, B.; Laduron, D.; Lasri, L. Petrology and Geodynamic Significance of the Post-Collisional Pan-African Magmatism in the Eastern Saghro Area (Anti-Atlas, Morocco). *J. Afr. Earth Sci.* **2009**, *55*, 105–124. [CrossRef]
64. Youbi, N.; Kouyaté, D.; Söderlund, U.; Ernst, R.E.; Soulaïmani, A.; Hafid, A.; Ikenne, M.; El Bahat, A.; Bertrand, H.; Rkha Chaham, K.; et al. The 1750 Ma Magmatic Event of the West African Craton (Anti-Atlas, Morocco). *Precambrian Res.* **2013**, *236*, 106–123. [CrossRef]
65. Baidada, B.; Cousens, B.; Alansari, A.; Soulaïmani, A.; Barbey, P.; Ilmen, S.; Ikenne, M. Geochemistry and Sm–Nd Isotopic Composition of the Imiter Pan-African Granitoids (Saghro Massif, Eastern Anti-Atlas, Morocco): Geotectonic Implications. *J. Afr. Earth Sci.* **2017**, *127*, 99–112. [CrossRef]
66. Thomas, R.J.; Chevallier, L.P.; Gresse, P.G.; Harmer, R.E.; Eglington, B.M.; Armstrong, R.A.; De Beer, C.H.; Martini, J.E.J.; De Kock, G.S.; Macey, P.H.; et al. Precambrian Evolution of the Sirwa Window, Anti-Atlas Orogen, Morocco. *Precambrian Res.* **2002**, *118*, 1–57. [CrossRef]
67. Gasquet, D.; Levresse, G.; Cheilletz, A.; Azizi-Samir, M.R.; Mouttaqi, A. Contribution to a Geodynamic Reconstruction of the Anti-Atlas (Morocco) during Pan-African Times with the Emphasis on Inversion Tectonics and Metallogenic Activity at the Precambrian–Cambrian Transition. *Precambrian Res.* **2005**, *140*, 157–182. [CrossRef]
68. Walsh, G.J.; Benziane, F.; Aleinikoff, J.N.; Harrison, R.W.; Yazidi, A.; Burton, W.C.; Quick, J.E.; Saadane, A. Neoproterozoic Tectonic Evolution of the Jebel Saghro and Bou Azzer—El Graara Inliers, Eastern and Central Anti-Atlas, Morocco. *Precambrian Res.* **2012**, *216–219*, 23–62. [CrossRef]
69. Youbi, N.; Ernst, R.E.; Söderlund, U.; Boumehdi, M.A.; Lahna, A.A.; Gaeta Tassinari, C.; El Moume, W.; Bensalah, M.K. The Central Iapetus Magmatic Province: An Updated Review and Link with the ca. 580 Ma Gaskiers Glaciation. *Spec. Pap. Geol. Soc. Am.* **2020**, *544*, 35–66. [CrossRef]
70. Paile, Y. Etude Des Séries Volcaniques Du Précambrien III de l’Ougnat (Anti-Atlas Oriental, Maroc) et Des Minéralisations Plombo-Zincifères Complexes Associées (Gîte de Bou Madine). Ph.D. Thesis, Université de Paris XI-Orsay, Paris, France, 1983.
71. Raddi, Y.; Tahiri, M.; Derré, C.; Lécolle, M. *Notice de La Carte Géologique d’Oukhit (Anti-Atlas, Maroc)*; Notes et Mémoires Service Géologique Maroc: Rabat, Morocco, 2006; 70p.
72. Soulaïmani, A.; Burkhard, M. The Anti-Atlas Chain (Morocco): The Southern Margin of the Variscan Belt along the Edge of the West African Craton. *Geol. Soc. Spec. Publ.* **2008**, *297*, 433–452. [CrossRef]
73. Destombes, J.; Hollard, H. Carte Géologique Du Maroc Au 1/200 000, Feuille Tafilalt-Taouz. In *Notes et Mémoires du Service Géologique du Maroc*; Editions du Service Géologique du Maroc: Rabat, Morocco, 1986; Volume 244.
74. Michard, A.; Hoepffner, C.; Soulaïmani, A.; Baidder, L. The Variscan Belt. In *Continental Evolution: The Geology of Morocco*; Part of the Book Series: Lecture Notes in Earth Sciences (LNEARTH); Springer: Berlin/Heidelberg, Germany, 2008; Volume 116, pp. 65–132. [CrossRef]
75. Destombes, J.; Hollard, H.; Willefert, S. Lower Palaeozoic Rocks of Morocco. In *Palaeoz. Rocks North-Western West-Central Africa*; Holland, C.H., Ed.; John Wiley: Chichester, UK, 1985; pp. 91–336.
76. Destombes, J.; Feist, R. Découverte Du Cambrien Supérieur En Afrique (Anti-Atlas Central, Maroc). *C. R. Acad. Sci.* **1987**, *304*, 719–724.

77. Baidder, L.; Raddi, Y.; Tahiri, M.; Michard, A. Devonian Extension of the Pan-African Crust North of the West African Craton, and Its Bearing on the Variscan Forelanddeformation: Evidence from Eastern Anti-Atlas (Morocco). *Geol. Soc. Spec. Publ.* **2008**, *297*, 453–465. [[CrossRef](#)]
78. Raddi, Y.; Derré, C.; Lécolle, M. Notice de La Carte Géologique de Bou Adil (Anti-Atlas, Maroc). In *Notes et Mémoires du Service Géologique du Maroc*; Editions du Service Géologique du Maroc: Rabat, Morocco, 2012; 70p.
79. Destombes, J.; Hollard, H. Carte Géologique Du Maroc Au 1:200 000. Feuille Todgha-Ma'der. In *Notes et Mémoires du Service Géologique du Maroc*; Editions du Service Géologique du Maroc: Rabat, Morocco, 1988; Volume 244.
80. Tahiri, M.; Derré, C.; Lécolle, M.; Baidder, L. Carte Géologique Du Maroc Au 1/50 000, Feuille d'Oukhit (Anti-Atlas, Maroc). In *Notes et Mémoires du Service Géologique du Maroc*; Editions du Service Géologique du Maroc: Rabat, Morocco, 2006.
81. Lalou, C.; Brichet, E.; Ku, T.L.; Jehanno, C. Radiochemical, Scanning Electron Microscope (SEM) and X-Ray Dispersive Energy (EDAX) Studies of a FAMOUS Hydrothermal Deposit. *Mar. Geol.* **1977**, *24*, 245–258. [[CrossRef](#)]
82. Creaser, R.A.; Gütter, H.; Carlson, J.; Crawford, B. Macrocrystal Phlogopite Rb–Sr Dates for the Ekati Property Kimberlites, Slave Province, Canada: Evidence for Multiple Intrusive Episodes in the Paleocene and Eocene. *Lithos* **2004**, *76*, 399–414. [[CrossRef](#)]
83. Holmden, C.; Creaser, R.A.; Muehlenbachs, K. Paleosalinities in Ancient Brackish Water Systems Determined by ⁸⁷Sr/⁸⁶Sr Ratios in Carbonate Fossils: A Case Study from the Western Canada Sedimentary Basin. *Geochim. Cosmochim. Acta* **1997**, *61*, 2105–2118. [[CrossRef](#)]
84. Poty, B.; Leroy, J.; Jachimowicz, L. Un Nouvel Appareil Pour La Mesure Des Températures Sous Le Microscope: L'installation de Microthermométrie Chaixmeca. *Bull. Minér.* **1976**, *99*, 182–186. [[CrossRef](#)]
85. Ulrich, M.R.; Bodnar, R.J. Systematics of Stretching of Fluid Inclusions II: Barite at 1 Atm Confining Pressure. *Econ. Geol.* **1988**, *83*, 1037–1046. [[CrossRef](#)]
86. Michard, A.-G. Sédiments-Temoin de La Transgression Mésozoïque Dans Le Tafilalt et Maïder; Conséquences Sur La Métallogénie Des Gisements Filoniens à Pn-Zn (Cu) de l'Anti-Atlas Marocain. *Chronique de la Recherche Minière* **1989**, *495*, 51–60.
87. Kharis, A.-A.; Ilmen, S.; Aissa, M.; Baidada, B.; Moussaid, A.; Mezougane, H.; Fadili, A.; Houane, H.; Syad, S.; Maacha, L. Metallogenesis of the Cu-Ni Sulfide Type Mineralization in the Bounhas Vein Deposit (Eastern Anti-Atlas, Morocco): Insights from Ore Mineral Paragenesis and Fluid Phases. *Sci. Afr.* **2023**, *21*, e01767. [[CrossRef](#)]
88. Claypool, G.E.; Holser, W.T.; Kaplan, I.R.; Sakai, H.; Zak, I. The Age Curves of Sulfur and Oxygen Isotopes in Marine Sulfate and Their Mutual Interpretation. *Chem. Geol.* **1980**, *28*, 199–260. [[CrossRef](#)]
89. Rddad, L.; Bouhlel, S. The Bou Dahar Jurassic Carbonate-Hosted Pb–Zn–Ba Deposits (Oriental High Atlas, Morocco): Fluid-Inclusion and C–O–S–Pb Isotope Studies. *Ore Geol. Rev.* **2016**, *72*, 1072–1087. [[CrossRef](#)]
90. Dumańska-Słowik, M.; Beata, N.; Toboła, T.; Powolny, T.; Huber, M.; Milovska, S.; Dobosz, N.; Guzik, K. Origin of Gem-Quality Barite at Jebel Ouichane District in Nador, Morocco: Implications from Integrated Fluid Inclusions, Stable Isotopes, and Geochemistry. *Res. Artic.* **2021**. [[CrossRef](#)]
91. Jébrak, M.; El Wartiti, M.; Marcoux, E.; Zaharoui, M. The Bouznika Cambrian Barite Deposit (Morocco), an Early Mineralization on the Iapetus Margin. *J. Afr. Earth Sci.* **2011**, *60*, 53–62. [[CrossRef](#)]
92. Roedder, E. *Fluid Inclusions: An Introduction to Studies of All Types of Fluid Inclusions, Gas, Liquid, or Melt, Trapped in Materials from Earth and Space, and Their Application to the Understanding of Geologic Processes*; Mineralogical Society of America: Chantilly, VA, USA, 1984; Volume 12, p. 644.
93. Shepherd, S.A.; Turner, J.A. Studies on Southern Australian Abalone (Genus *Haliotis*). VI. Habitat Preference, Abundance and Predators of Juveniles. *J. Exp. Mar. Biol. Ecol.* **1985**, *93*, 285–298. [[CrossRef](#)]
94. Sterner, S.M.; Hall, D.L.; Bodnar, R.J. Synthetic Fluid Inclusions. V. Solubility Relations in the System NaCl-KCl-H₂O under Vapor-Saturated Conditions. *Geochim. Cosmochim. Acta* **1988**, *52*, 989–1005. [[CrossRef](#)]
95. Goldstein, R.J.; Jabbari, M.Y.; Chen, S.B. Convective Mass Transfer and Pressure Loss Characteristics of Staggered Short Pin-Fin Arrays. *Int. J. Heat Mass Transf.* **1994**, *37*, 149–160. [[CrossRef](#)]
96. Hanor, J.S. Origin of Saline Fluids in Sedimentary Basins. *Geol. Soc. Spec. Publ.* **1994**, *78*, 151–174. [[CrossRef](#)]
97. Barbieri, M.; Bellanca, A.; Neri, R.; Tolomeo, L. Use of Strontium Isotopes to Determine the Sources of Hydrothermal Fluorite and Barite from Northwestern Sicily (Italy). *Chem. Geol. Isot. Geosci. Sect.* **1987**, *66*, 273–278. [[CrossRef](#)]
98. Chen, H. External Sulphur in IOCG Mineralization: Implications on Definition and Classification of the IOCG Clan. *Ore Geol. Rev.* **2013**, *51*, 74–78. [[CrossRef](#)]
99. Dora, M.L.; Roy, S.K.; Khan, M.; Randive, K.; Kanungo, D.R.; Barik, R.; Kaushik, C.S.; Bari, S.H.; Pattanayak, R.S.; Krishna, K.V.S.; et al. Rift-Induced Structurally Controlled Hydrothermal Barite Veins in 1.6 Ga Granite, Western Bastar Craton, Central India: Constraints from Fluid Inclusions, REE Geochemistry, Sulfur and Strontium Isotopes Studies. *Ore Geol. Rev.* **2022**, *148*. [[CrossRef](#)]
100. Kesler, S.; Jones, L.; Ruiz, J. Strontium Isotopic Geochemistry of Mississippi Valley-Type Deposits, East Tennessee: Implications for Age and Source of Mineralizing Brines. Available online: <https://pubs.geoscienceworld.org/gsa/gsbulletin/article-abstract/10/0/8/1300/182201/Strontium-isotopic-geochemistry-of-Mississippi> (accessed on 2 August 2023).
101. Marchev, P.; Downes, H.; Thirlwall, M.F.; Moritz, R. Small-Scale Variations of ⁸⁷Sr/⁸⁶Sr Isotope Composition of Barite in the Madjarovo Low-Sulphidation Epithermal System, SE Bulgaria: Implications for Sources of Sr, Fluid Fluxes and Pathways of the Ore-Forming Fluids. *Min. Miner. Depos.* **2002**, *37*, 669–677. [[CrossRef](#)]
102. Kontak, D.J.; Kyser, K.; Gize, A.; Marshall, D. Structurally Controlled Vein Barite Mineralization in the Maritimes Basin of Eastern Canada: Geologic Setting, Stable Isotopes, and Fluid Inclusions. *Econ. Geol.* **2006**, *101*, 407–430. [[CrossRef](#)]

103. Staude, S.; Göb, S.; Pfaff, K.; Ströbele, F.; Premo, W.R.; Markl, G. Deciphering Fluid Sources of Hydrothermal Systems: A Combined Sr- and S-Isotope Study on Barite (Schwarzwald, SW Germany). *Chem. Geol.* **2011**, *286*, 1–20. [[CrossRef](#)]
104. Mao, J.W.; Zhang, Z.C.; Yang, J.M.; Zuo, G.C.; Zhang, Z.H.; Ye, D.J.; Jiang, M. *The Metallogenic Series and Prospecting Assessment of Copper, Gold, Iron and Tungsten Polymetallic Ore Deposits in the West Sector of the Northern Qilian Mountains*; Geological Publishing House: Beijing, China, 2003; pp. 157–242.
105. Lydon, J.W. Volcanogenic Massive Sulphide Deposits, Part 1 A Descriptive Model. *Geosci. Can.* **1984**, *11*, 195–202.
106. Groves, D.I.; Goldfarb, R.J.; Robert, F.; Hart, C.J.R. Gold Deposits in Metamorphic Belts: Overview of Current Understanding, Outstanding Problems, Future Research, and Exploration Significance. *Econ. Geol.* **2003**, *98*, 1–29. [[CrossRef](#)]
107. Brusnitsyn, A.I.; Sadykov, S.A.; Perova, E.N.; Vereshchagin, O.S. Genesis of Barite–Galena Ores at the Ushkatyn-III Deposit, Central Kazakhstan: Analysis of Geological, Mineralogical, and Isotopic ($\Delta^{34}\text{S}$, $\Delta^{13}\text{C}$, $\Delta^{18}\text{O}$) Data. *Geol. Ore Depos.* **2022**, *64*, 78–103. [[CrossRef](#)]
108. Outigua, A.; Essaifi, A.; Corsini, M.; Outhounjite, M.; Zouhair, M. Sidi m'barek: A Representative Example of the Moroccan Massive Sulfide Deposits. In *Geological Society Special Publication*; Geological Society of London: London, UK, 2021; Volume 502, pp. 67–95.
109. Walter, B.F.; Jensen, J.L.; Coutinho, P.; Laurent, O.; Markl, G.; Steele-MacInnis, M. Formation of Hydrothermal Fluorite-Hematite Veins by Mixing of Continental Basement Brine and Redbed-Derived Fluid: Schwarzwald Mining District, SW-Germany. *J. Geochem. Explor.* **2020**, *212*. [[CrossRef](#)]
110. Zou, H.; Li, M.; Santosh, M.; Zheng, D.; Cao, H.-w.; Jiang, X.W.; Chen, H.F.; Li, Z. Fault-Controlled Carbonate-Hosted Barite-Fluorite Mineral Systems: The Shuanghe Deposit, Yangtze Block, South China. *Gondwana Res.* **2021**, *101*, 26–43. [[CrossRef](#)]
111. Alaminia, Z.; Tadayan, M.; Griffith, E.M.; Solé, J.; Corfu, F. Tectonic-Controlled Sediment-Hosted Fluorite-Barite Deposits of the Central Alpine-Himalayan Segment, Komsheche, NE Isfahan, Central Iran. *Chem. Geol.* **2021**, *566*. [[CrossRef](#)]
112. Veizer, J.; Hoef, J.; Lowe, D.R.; Thurston, P.C. Geochemistry of Precambrian Carbonates: II. Archean Greenstone Belts and Archean Sea Water. *Geochim. Cosmochim. Acta* **1989**, *53*, 859–871. [[CrossRef](#)] [[PubMed](#)]
113. Deb, M.; Hoefs, J.; Bauman, A. Isotopic Composition of Two Precambrian Stratiform Barite Deposits from the Indian Shield. *Geochim. Et Cosmochim. Acta* **1991**, *55*, 303–308. [[CrossRef](#)]
114. Galindo, C.; Tornos, F.; Darbyshire, D.P.F.; Casquet, C. The Age and Origin of the Barite-Fluorite (Pb-Zn) Veins of the Sierra Del Guadarrama (Spanish Central System, Spain): A Radiogenic (Nd, Sr) and Stable Isotope Study. *Chem. Geol.* **1994**, *112*, 351–364. [[CrossRef](#)]
115. Matter, A.; Peters, T.; Ramseyer, K. $^{87}\text{Sr}/^{86}\text{Sr}$ -Verhältnisse Und Sr-Gehalte von Tiefengrundwässern, Mineralien Sowie Gesteinen Aus Dem Kristallin Und Der Trias Der Nordschweiz. *Eclogae Geol. Helv.* **1987**, *80*, 579–592.
116. Hofmann, R.; Baumann, A. Preliminary Report on the Sr Isotopic Composition of Hydrothermal Vein Barites in the Federal Republic of Germany. *Min. Miner. Depos.* **1984**, *19*, 166–169. [[CrossRef](#)]
117. Maynard, J.B.; Morton, J.; Valdes-Nodarse, E.L.; Diaz-Carmona, A. Sr Isotopes of Bedded Barites; Guide to Distinguishing Basins with Pb-Zn Mineralization. *Econ. Geol.* **1995**, *90*, 2058–2064. [[CrossRef](#)]
118. Chaudhuri, S.; Clauer, N. Strontium Isotopic Compositions and Potassium and Rubidium Contents of Formation Waters in Sedimentary Basins: Clues to the Origin of the Solutes. *Geochim. Cosmochim. Acta* **1993**, *57*, 429–437. [[CrossRef](#)]
119. Mauriohoo, K.; Barker, S.L.L.; Rae, A. Mapping Lithology and Hydrothermal Alteration in Geothermal Systems Using Portable X-Ray Fluorescence (PXRF): A Case Study from the Tauhara Geothermal System, Taupo Volcanic Zone. *Geothermics* **2016**, *64*, 125–134. [[CrossRef](#)]
120. McNutt, R.H.; Frape, S.K.; Fritz, P.; Jones, M.G.; MacDonald, I.M. The $^{87}\text{Sr}/^{86}\text{Sr}$ Values of Canadian Shield Brines and Fracture Minerals with Applications to Groundwater Mixing, Fracture History, and Geochronology. *Geochim. Cosmochim. Acta* **1990**, *54*, 205–215. [[CrossRef](#)]
121. Hedenquist, J.W.; Henley, R.W. The Importance of CO₂ on Freezing Point Measurements of Fluid Inclusions: Evidence from Active Geothermal Systems and Implications for Epithermal Ore Deposition. *Econ. Geol.* **1985**, *80*, 1379–1406. [[CrossRef](#)]
122. Potter, R.; Robert, W.; Brown, D. The Volumetric Properties of Aqueous Sodium Chloride Solutions from 00 to 5000C at Pressures up to 2000 Bars Based on a Regression of Available Data in the Literature. *Geol. Surv. Bull.* **1977**, *1421*, 1–36.
123. Walter, B.F.; Kortenbruck, P.; Scharrer, M.; Zeitvogel, C.; Wälle, M.; Mertz-Kraus, R.; Markl, G. Chemical Evolution of Ore-Forming Brines—Basement Leaching, Metal Provenance, and the Redox Link between Barren and Ore-Bearing Hydrothermal Veins. A Case Study from the Schwarzwald Mining District in SW-Germany. *Chem. Geol.* **2019**, *506*, 126–148. [[CrossRef](#)]
124. Favre, P.; Stampfli, G.M. From Rifting to Passive Margin: The Examples of the Red Sea, Central Atlantic and Alpine Tethys. *Tectonophysics* **1992**, *215*, 69–97. [[CrossRef](#)]
125. Emery, K.O.; Uchupi, E. *The SYN-RIFT Supersequence and Crustal Boundary. The Geology of the Atlantic Ocean*; Springer: New York, NY, USA, 1984; pp. 263–367. [[CrossRef](#)]
126. Cardellach López, E.; Canals i Sabaté, À.; Tritlla i Cambra, J. Late and Post-Hercynian Low Temperature Veins in the Catalonian Coastal Ranges. *Acta Geol. Hisp.* **1990**, *25*, 0075–0081.
127. Carignan, J.; Gariépy, C.; Hillaire-Marcel, C. Hydrothermal Fluids during Mesozoic Reactivation of the St. Lawrence Rift System, Canada: C, O, Sr and Pb Isotopic Characterization. *Chem. Geol.* **1997**, *137*, 1–21. [[CrossRef](#)]
128. Tornos, F.; Spiro, B.F. The Geology and Isotope Geochemistry of the Talc Deposits of Puebla de Lillo (Cantabrian Zone, Northern Spain). *Econ. Geol.* **2000**, *95*, 1277–1296. [[CrossRef](#)]
129. Boni, M.; Muchez, P.; Schneider, J. Permo-Mesozoic Multiple Fluid Flow and Ore Deposits in Sardinia: A Comparison with Post-Variscan Mineralization of Western Europe. *Geol. Soc. Spec. Publ.* **2002**, *204*, 199–211. [[CrossRef](#)]

130. Haschke, S.; Gutzmer, J.; Wohlgemuth-Ueberwasser, C.C.; Kraemer, D.; Burisch, M. The Niederschlag Fluorite-(Barite) Deposit, Erzgebirge/Germany—A Fluid Inclusion and Trace Element Study. *Min. Miner. Depos.* **2021**, *56*, 1071–1086. [[CrossRef](#)]
131. Burisch, M.; Markl, G.; Gutzmer, J. Breakup with Benefits—Hydrothermal Mineral Systems Related to the Disintegration of a Supercontinent. *Earth Planet. Sci. Lett.* **2022**, *580*, 117373. [[CrossRef](#)]

Disclaimer/Publisher’s Note: The statements, opinions and data contained in all publications are solely those of the individual author(s) and contributor(s) and not of MDPI and/or the editor(s). MDPI and/or the editor(s) disclaim responsibility for any injury to people or property resulting from any ideas, methods, instructions or products referred to in the content.